Published in final edited form as:
*Nat Neurosci*. 2015 September ; 18(9): 1281–1290. doi:10.1038/nn.4074.

# Determinants of different deep and superficial CA1 pyramidal cell dynamics during sharp-wave ripples

**Manuel Valero**[#1], **Elena Cid**[#1], **Robert G Averkin**[#2], **Juan Aguilar**[3], **Alberto Sanchez-Aguilera**[1,4], **Tim J Viney**[5], **Daniel Gomez-Dominguez**[1], **Elisa Bellistri**[1], and **Liset Menendez de la Prida**[1]

[1]Instituto Cajal, Consejo Superior de Investigaciones Científicas, Madrid, Spain

[2]Hungarian Academy of Sciences, University of Szeged Research Group for Cortical Microcircuits, Department of Physiology, Anatomy and Neuroscience, University of Szeged, Szeged, Hungary

[3]Hospital Nacional de Parapléjicos, Servicio de Salud de Castilla-La Mancha, Toledo, Spain

[4]Departamento de Fisiología, Facultad de Medicina, Universidad Complutense, Madrid, Spain

[5]Medical Research Council Brain Network Dynamics Unit, Department of Pharmacology, University of Oxford, Oxford, UK

[#] These authors contributed equally to this work.

## Abstract

Sharp-wave ripples represent a prominent synchronous activity pattern in the mammalian hippocampus during sleep and immobility. GABAergic interneuronal types are silenced or fire during these events, but the mechanism of pyramidal cell (PC) participation remains elusive. We found opposite membrane polarization of deep (closer to stratum oriens) and superficial (closer to stratum radiatum) rat CA1 PCs during sharp-wave ripples. Using sharp and multi-site recordings in combination with neurochemical profiling, we observed a predominant inhibitory drive of deep calbindin (CB)-immunonegative PCs that contrasts with a prominent depolarization of superficial CB-immunopositive PCs. Biased contribution of perisomatic GABAergic inputs, together with suppression of CA2 PCs, may explain the selection of CA1 PCs during sharp-wave ripples. A deep-superficial gradient interacted with behavioral and spatial effects to determine cell participation during sleep and awake sharp-wave ripples in freely moving rats. Thus, the firing



Correspondence should be addressed to L.M.d.l.P. (lmprida@cajal.csic.es).

**AUTHOR CONTRIBUTIONS**

J.A. and L.M.d.l.P. first observed the phenomenon. L.M.d.l.P. designed and coordinated the study. M.V., J.A. and L.M.d.l.P. obtained *in vivo* sharp recordings. A.S.-A. and L.M.d.l.P. performed *in vitro* experiments. M.V. and R.G.A. obtained recordings from freely moving rats. E.C. was responsible for the immunohistological characterization of recorded cells. M.V. and T.J.V. were responsible for identification and quantification of perisomatic GABAergic boutons. M.V., E.C., A.S.-A., T.J.V., E.B., D.G.-D. and L.M.d.l.P. analyzed and interpreted the data. L.M.P. wrote the paper.

Note: Any Supplementary Information and Source Data files are available in the online version of the paper.

**COMPETING FINANCIAL INTERESTS**

The authors declare no competing financial interests.

A Supplementary methods checklist is available.


Europe PMC Funders Author Manuscripts

dynamics of hippocampal PCs are exquisitely controlled at subcellular and microcircuit levels in a cell type–selective manner.

Sharp waves (SPWs) are transient events recorded in the local field potentials of the mammalian hippocampus during periods of immobility, slow-wave sleep and anesthesia[1,2]. They are maximally expressed in the CA1 stratum radiatum and presumably reflect net dendritic depolarization of CA1 PCs activated by the Schaffer collaterals of discharging CA3 neurons[3,4]. In close temporal association with SPWs, high-frequency oscillations (ripples, 90–200 Hz) are confined around the stratum pyramidale, where they are likely to reflect phase-locked firing of CA1 PCs curtailed by fast runs of feedforward and feedback inhibitory potentials (IPSPs)[1,5]. A plethora of hippocampal GABAergic interneuronal types exhibit specific phase-locked firing or are silent during SPW events[6,7]. Excitatory and inhibitory potentials therefore compete to control spike timing of principal glutamatergic neurons[8,9].

The CA1 stratum pyramidale of the dorsal hippocampus can be differentiated into deep and superficial layers on the basis of cell density[10], gene expression[11], immunoreactivity to CB[12] and the different shapes of PCs[13]. During development, CA1 PCs express genes (*Sox5, SatB2, Zbtb20*) that are known to specify the phenotypes of superficial and deep cells in the neocortex[10,14]. All CA1 PCs are innervated directly by Schaffer collaterals from both the ipsilateral and contralateral CA3, but CA2 PCs activate deep CB-negative CA1 PCs preferentially[15]. Local GABAergic microcircuits discriminate between deep and superficial sublayers and distinctly regulate ventral hippocampal interaction with the amygdala and the prefrontal cortex[16]. Functional differences between PCs in these two sublayers have been shown to emerge in periods of theta oscillations associated with exploration and REM sleep[17] and during gamma activity accompanying theta[18]. In contrast, during SPW ripples, putative deep and superficial CA1 PCs appear to similarly participate and only a proportion of deep cells (that is, REM-shifting neurons) respond strongly[17]. More recently, silicon shank recordings have revealed a different entrainment of deep and superficial PCs during SPW ripples[19]. However, these extracellular recordings are biased toward subpopulations of firing cells, some of which are spatially modulated during these synchronous events[20], and poorly inform on their subthreshold dynamics or detailed molecular phenotype.

Using a combination of intracellular, extracellular and multi-site recordings and stimulation in conjunction with *post hoc* immunolabeling, we successfully identified a variety of PCs from the dorsal hippocampus of both anesthetized and freely moving rats. Our data unveil the mechanisms underlying the heterogeneous behavior of deep and superficial CA1 PCs during spontaneous SPW ripple events. We found an exquisitely controlled microcircuit operation of CA1 PCs that challenges the view of hippocampal dynamics during these events.




Europe PMC Funders Author Manuscripts

# RESULTS

## Heterogeneous intracellular dynamics of deep and superficial CA1 PCs

We combined sharp and 16-channel multi-site recordings in conjunction with *post hoc* immunohistochemistry to identify the intracellular dynamics and the molecular identity of CA1 PCs from the dorsal hippocampus of urethane anesthetized rats ($n$ = 22 CA1 PCs; Fig. 1a,b, Supplementary Fig. 1a and Supplementary Table 1). Notably, we observed two opposite intracellular behaviors of CA1 PCs at the SPW peak recorded in the stratum radiatum: a net depolarization (4.1 ± 2.3-mV peak response, $n$ = 12; Fig. 1c) and hyperpolarization (−2.4 ± 1.2-mV peak response, $n$ = 10; Fig. 1d) at similar resting membrane potentials (depolarized CA1 PCs: −63.8 ± 5.1 mV; hyperpolarized PCs: −61.4 ± 2.9 mV; $P$ = 0.176, $t(20)$ = 1.68; unpaired $t$ test). Intracellular responses were systematic across several SPWs for a given cell. Contralateral (cCA3; ipsilateral, iCA3; Fig. 1e and Supplementary Fig. 1b) electrical stimulation of the upstream CA3 region reproduced this behavior for stimulation intensities lower than 500 μA (cCA3: 11 depolarized/7 hyperpolarized, $P$ = 0.019, $F(1.22, 3.69)$ = 15.24; iCA3: 4 depolarized/4 hyperpolarized, $P$ = 0.060, $F(1.07, 4.27)$ = 6.33; repeated-measures ANOVA; Fig. 1c,d), suggesting that it reflects feedforward responses, as confirmed by local pharmacology (Supplementary Fig. 1c–e). Holding membrane potentials at several levels revealed similar reversal for the cCA3-evoked and the SPW-associated responses in a given cell (Fig. 1c,d), and also revealed differences between cell groups (Fig. 1f). The corresponding driving force was also different between groups (SPW-associated: $P$ < 0.0001, $t(19)$ = 7.85; cCA3-evoked: $P$ = 0.0001, $t(16)$ = 5.09; unpaired $t$ test for 11 depolarized/10 hyperpolarized; Fig. 1g). The SPW-associated reversal potential of hyperpolarized cells was −65.9 ± 4.4 mV, relatively close to that of $GABA_A$-receptor reversal (−70 mV), whereas, in depolarized cells, the reversal potential was −58.6 ± 4.8 mV, reflecting a synaptic mixture of excitatory and inhibitory inputs. Note that the reversal potential of depolarized cells ensures that their firing will be modulated during suprathreshold current injections, as recently shown[9].

We next addressed the intracellular correlation with the SPW and ripple components of associated events. Although the direction of the intracellular responses was consistent across events, their amplitudes were variable. To evaluate this further, we used data from a subset of cells with current source–density (CSD) signals spanning from the CA1 stratum pyramidale to the stratum lacunosum moleculare and a sufficient number of events at resting membrane potential ($n$ = 7 depolarized, $n$ = 7 hyperpolarized). We estimated the SPW-associated CSD sinks and sources known to reflect transmembrane currents flowing through the somatodendritic compartments[3,5] (Supplementary Fig. 2a). The peak amplitude of the intracellular response measured at resting membrane potential and the SPW-associated sink at the stratum radiatum were strongly correlated event-to-event in depolarized, but not in hyperpolarized, PCs ($P$ = 0.0012, $\chi^2$ (3.14) = 10.50; $\chi^2$ test; Supplementary Fig. 2b). No difference in mean CSD amplitude accounted for this effect ($P$ = 0.9671, $t(12)$ = −0.04 for SR sinks; $P$ = 0.5651, $t(12)$ = −0.59 for stratum radiatum sources; unpaired $t$ test; Supplementary Fig. 2a). There was poor correlation between the intracellular response and the SPW-associated source at the stratum pyramidale ($P$ = 0.5148, $\chi^2$ (3.14) = 0.42, $\chi^2$ test;

Supplementary Fig. 2c), in spite of strong covariations in the magnitude of the sink and the sources (Supplementary Fig. 2d).

We then evaluated whether intracellular subthreshold oscillations associated with ripples recorded in the stratum pyramidale[5,8] were differentially correlated in these two groups ($n$ = 12 depolarized, $n$ = 9 hyperpolarized; Fig. 2 and Supplementary Fig. 3). At resting membrane potential, we found that barrages of intracellular synaptic activity contributed to a dominant spectral peak at the 90–200-Hz band in close association with extracellular ripples (Fig. 2a–d). Notably, the power of the intracellular ripple was significantly smaller in depolarized versus hyperpolarized CA1 PCs ($P$ = 0.0124, $t(19)$ = −2.76, unpaired $t$ test; Fig. 2e). A cross-correlation index between intracellular and extracellular ripples (Supplementary Fig. 3b) suggested lower interaction in depolarized cells ($P$ = 0.0147, $t(19)$ = −2.68, unpaired $t$ test; Fig. 2e). This was not dependent on the holding membrane potential (Supplementary Fig. 3c) nor on the distance to the extracellular probe, as confirmed in a subset of experiments (depolarized: 510 ± 347 μm, $n$ = 9; hyperpolarized: 417 ± 170 μm, $n$ = 5; $P$ = 0.5892, $t(12)$ = 0.55; unpaired $t$ test; Fig. 2f). Thus, extracellular signatures of associated ripples more likely reflect intracellular high-frequency synaptic activity (presumably IPSPs–excitatory post-synaptic potentials (EPSPs)) of hyperpolarized CA1 PCs. Together these data indicate heterogeneous contribution of CA1 PCs to spontaneous SPW-ripple events recorded in the rat dorsal hippocampus.

## Anatomical determinants of CA1PC heterogeneity

We next looked for anatomical determinants of this heterogeneity in a subset of successfully labeled cells ($n$ = 11 depolarized, $n$ = 7 hyperpolarized; Fig. 3a). We did not find an anteroposterior ($P$ = 0.6713, $t(16)$ = −0.43, unpaired $t$ test) or mediolateral ($P$ = 0.7262, $t(16)$ = 0.35, unpaired $t$ test) effect in cell location or on their linear distance to CA2 ($P$ = 0.9159, $t(16)$ = −0.11, unpaired $t$ test; Supplementary Table 1). In contrast, there was a strong effect of cell distance to the border with stratum radiatum ($P$ = 0.0152, $t(16)$ = −2.72, unpaired $t$ test), with depolarized cells more typically being located closer (superficial layer) and hyperpolarized cells being located more distant (deep layers; Fig. 3b). This distribution at the single-cell level matched well with CB expression in the CA1 stratum pyramidale ($P$ = 0.0483, $r(16)$ = −0.4713, Pearson correlation; Supplementary Fig. 4). Depolarized CA1 PCs displayed varying levels of CB immunoreactivity (8 of 11 PCs; Fig. 3b,c), whereas most hyperpolarized cells (5 of 7) lacked detectable immunoreactivity ($P$ = 0.0660, $\chi^2$ (3.18) = 3.38, $\chi^2$ test; Fig. 3b,d). Some depolarized CA PCs were CB-immunonegative (Fig. 3e). To gain further insight into the mechanisms surrounding different hyperpolarized and depolarized responses, we compared the CB immunoreactivity and position in the pyramidal layer for each recorded cell to their SPW-associated reversal potential and driving force (Supplementary Table 1). The distribution of reversal potential values along the distance to stratum radiatum suggested a continuum (Fig. 3f). Notably, deep-superficial criteria revealed significant differences (deep: −63.2 ± 4.1 mV; superficial: −58.8 ± 5.0 mV; $P$ = 0.0405, $t(16)$ = 1.86, unpaired $t$ test), but these were marginal when cells were classified according to their CB immunoreactivity resulting from dispersion (Fig. 3f). In contrast, the SPW-associated driving force exhibited clear differences between groups by clustering reversal potential values relative to the resting membrane potential (Fig. 3g). Driving force data were

significantly different for deep (−2.41 ± 3.56 mV) and superficial PCs (4.18 ± 4.62 mV; $P$ = 0.0135, rank sum = 140, Mann-Whitney test), but again remained marginally different for CB classification (Fig. 3g). These data indicate a laminar orthogonalization of intracellular dynamics along the hippocampal CA1 stratum pyramidale. What are the mechanisms underlying such a laminar dependence?

Given the strong correlation between the radiatum SPW sink and the intracellular response in depolarized, but not in hyperpolarized, PCs, and our reversal and driving force data, we reasoned that perisomatic GABAergic inhibition could unequally dominate the intracellular dynamics. To determine whether this factor accounts for opposite intracellular behavior, we examined the localization of gephyrin in GABAergic postsynaptic sites[21] to evaluate perisomatic GABAergic inhibition quantitatively. Lack of gephyrin immunoreactivity in recorded cells prevented us from analyzing these signals on a single-cell basis (Supplementary Fig. 5), and we instead adopted a population approach. We focused on GABAergic boutons derived from basket cells that were immunoreactive to parvalbumin (PV) and cholecystokinin (CCK) and known to mediate the major perisomatic inhibitory signaling in CA1 (ref. 22). Thus, we stereologically evaluated the density of gephyrin-immunoreactive puncta that colocalized with presynaptic PV and the CCK-specific cannabinoid receptor CB1R[23] on PCs visualized with the CA1-specific marker Wfs1 (Fig. 4a–c). We found more abundant perisomatic PV+ GABAergic boutons in deep CA1 PCs ($n$ = 34 cells from 4 confocal stacks from 3 rats, $P$ = 0.0162, $r(32)$ = 0.39, Pearson correlation; Fig. 4d) and a marked inverse correlation with CB1R boutons, which were densest at superficial CA1 PCs ($P$ = 0.0046, $r(32)$ = −0.46, Pearson correlation; Fig. 4e). There was no trend when PV+ and CB1R+ boutons were considered together ($P$ = 0.5415, $r(32)$ = −0.18, Pearson correlation). It should be noted that, although the overwhelming majority of specifically somatic boutons on CA1 pyramidal cells are from PV and CCK basket cells[24], other perisomatic regions (such as the proximal dendrites) receive other GABAergic inputs[22]. Thus, uneven contribution of feedforward GABAergic inhibition mediated by PV+ and CCK+ basket cells following deep and superficial PCs could potentially explain functional differences during SPW ripples. In addition, a dominant inhibitory drive at perisomatic compartments of deep CA1 PCs could be masking visibility of dendritic glutamatergic potentials activated by upstream hippocampal principal cells.

## Mechanisms of CA1 PC heterogeneity *in vitro*

To examine this point further, we prepared sagittal slices from juvenile (P15–25, $n$ = 38) and adult rats (P39–58, $n$ = 5) to evaluate synaptic responses of dorsal CA1 PCs to CA3 stimulation with patch-clamp recordings (Fig. 5a). CA1 PCs in deep and superficial layers were visually identified and their location was confirmed by complementary tests for CB immunoreactivity (Fig. 5b and Online Methods). Mild stimulation intensity of Schaffer collaterals was adjusted to elicit comparable extracellular responses in slices used to record deep and superficial cells ($P$ = 0.6831, $t(18)$ = 0.41; unpaired $t$ test; 12 superficial/8 deep CA1 PCs; Fig. 5c), mimicking *in vivo* experiments (Supplementary Fig. 1b).

Similar to that reported *in vivo*, we found dominant hyperpolarized responses to CA3 stimulation in deep ($n$ = 8) versus superficial CA1 PCs ($n$ = 12) at resting membrane

potential in current-clamp conditions (Fig. 5d). We evaluated evoked synaptic currents (EPSC, ISPC) elicited in deep and superficial CA1 PCs using voltage-clamp conditions at different holding potentials (Fig. 5d and Supplementary Fig. 6a). Significant differences were detected between cell types for the amplitude of IPSCs recorded at +10 mV ($P$ = 0.0021, $t(18)$ = 3.39, unpaired $t$ test; Fig. 5e), which were strongly correlated with the cell distance to radiatum ($P$ < 0.0001, $r(18)$ = 0.76; Pearson correlation; Fig. 5f). There was no statistical difference on the amplitude of the EPSC at −70 mV ($P$ = 0.2221, $t(18)$ = 1.266, unpaired $t$ test; Fig. 5e), but we did observe a mild spatial correlation ($P$ = 0.0358, $r(18)$ = 0.47, Pearson correlation; Fig. 3f). Similar results were obtained for IPSCs and EPSCs measured at −50 mV (Supplementary Fig. 6b). No correlation with age was detected (EPSC: $P$ = 0.3191, $r(41)$ = −0.15; IPSC: $P$ = 0.5891, $r(41)$ = 0.08; Pearson correlation). Blockage of glutamatergic transmission with CNQX (20 μM) and AP5 (50 μM) confirmed the feedforward nature of GABAergic IPSCs ($n$ = 6 deep, $n$ = 6 superficial; Supplementary Fig. 6c). We also considered the possibility that a different timing between excitation and inhibition ($\Delta t$) could contribute to functional differences between deep and superficial PCs (Supplementary Fig. 6d). Although no difference in the onset of the EPSCs and IPSCs survived in comparisons between groups (Supplementary Fig. 6d), they accumulated to show significant differences in $\Delta t$ in deep versus superficial PCs ($P$ = 0.0431, $t(18)$ = 2.18, unpaired $t$ test; Fig. 5g). Thus, a shorter time window of opportunity between excitation and inhibition, together with stronger inhibition of deep CA1 PCs, support their dominant inhibitory drive in response to CA3 activation.

What is the nature of the dominant feedforward inhibition in deep CA1 PCs? Our gephyrin-associated presynaptic bouton counts suggest that PV-mediated perisomatic inhibition should dominate in deep cells. We tested this point directly by measuring IPSCs at −50 mV while stimulating the stratum pyramidale extracellularly in the presence of glutamate and GABAb receptor antagonists. Consistent with our previous data, deep CA1 PCs ($n$ = 5) exhibited larger IPSCs at −50 mV than superficial cells ($n$ = 4, $P$ = 0.0061, $t(7)$ = −3.872, unpaired $t$ test; Fig. 5h) and we observed a positive correlation with the distance to radiatum ($P$ = 0.0012, $r(7)$ = 0.82, Pearson correlation; Fig. 5i). Suppressing GABAergic release from PV+ basket cells with DAMGO (200 nM)[25] confirmed that there was a larger contribution from deep cells than superficial cells (IPSC reduction in deep: 50.1 ± 5.1%; superficial: 29.3 ± 7.2%; $P$ = 0.0284, $t(4)$ = 3.981, paired $t$ test), consistent with our gephyrin data (Fig. 5i). Consistently, differences between cell groups were abolished by DAMGO ($P$ = 0.115, $t(7)$ = −3.872, unpaired $t$ test). However, although the correlation between IPSC amplitude and the distance to radiatum was reduced by DAMGO, it was still positive ($P$ = 0.0131, $r(7)$ = 0.78, Pearson correlation; Fig. 5i), suggesting that the opposite trend by CCK innervation (Fig. 4e) was not enough to compensate for an overall predominant inhibition of deep CA1 PCs. Functional differences between PV- and CCK-mediated perisomatic inhibition in terms of fluctuations of amplitude, latency and fidelity of unitary IPSCs could also contribute[26]. Further suppressing GABA release from CCK+ basket cells with WIN55-212 (5 μM)[23] occluded the relationship with distance to radiatum ($P$ = 0.0610, Pearson correlation; Fig. 5i).

We also examined the CA2-CA1 circuitry, given its preference for deep CA1 layer, as determined optogenetically in mice[15]. To this purpose we constrained mild extracellular

stimulation to the CA2 stratum pyramidale, as confirmed with immunolabeling against the CA2-specific marker PCP4, while recording from deep ($n = 5$) and superficial CA1 PCs ($n = 7$; Fig. 5j). Both cell types responded with strong disynaptic inhibition following CA2 stimulation, but deep cells were able to fire during some sweeps, as tested in current clamp (Fig. 5k). Estimation of the evoked ESPC amplitude at −70 mV confirmed stronger glutamatergic activation of deep cells ($P = 0.0474$, $t(10) = -2.259$, unpaired $t$ test; Fig. 5l). Consistent with stronger local perisomatic inhibition of deep CA1 cells, differences were also detected in IPSCs recorded at +10 mV ($P = 0.0007$, $t(10) = 4.813$, unpaired $t$ test; Fig. 5l). This trend persisted for EPSCs and IPSCs recorded at −50 mV, but large variability prevented statistical differences (Supplementary Fig. 6e). Finally, given that activation of CA2 PCs by CA3 terminals would affect the operation of the CA3-CA1 microcircuit, we also examined their response to CA3 stimulation *in vitro* (Fig. 5j). Consistent with previous reports[27], CA3-CA2 synapses were dominated by strong feedforward inhibition that typically prevented CA2 PC firing ($n = 3$; Fig. 5l,m).

## Microcircuit control of CA1 PC responses *in vivo*

We further tested the CA3-CA2 microcircuit *in vivo* by recording PCs intracellularly. All CA3c PCs ($n = 4$) exhibited depolarization well before SPW ripple events recorded with 16-channel arrays in CA1 and often reached the threshold for firing at resting membrane potentials (driving force 0.6 ± 0.3 mV, $V_{rev}$ −59.2 ± 7.9 mV; Fig. 6a). Their identity was confirmed by their typical response to both ipsi- (data not shown) and contralateral CA3 stimulation, including antidromic activation, and after visualization of Neurobiotin labeling with DAB-HRP reaction (Fig. 6a). In contrast, all CA2 PCs ($n = 3$) exhibited a dominant hyperpolarizing drive during spontaneous SPW ripples recorded in CA1 (driving force −3.2 ± 0.5 mV, $V_{rev}$ −62.4 ± 2.1 mV; Fig. 6b). The identity of CA2 PCs was confirmed with PCP4 immunolabeling (Fig. 6b). Consistent with *in vitro* data, CA2 PCs were predominantly inhibited by contralateral (data not shown) and ipsilateral CA3 stimulation (driving force −3.9 ± 1.3 mV, $V_{rev}$ −63.1 ± 1.4 mV; Fig. 6b).

Next, we evaluated the firing dynamics of different hippocampal PCs along the cornu ammonis during SPW ripples recorded at CA1 by constructing peri-event firing histograms of the different cell types recorded at resting membrane potential for a sufficient number of events (that is, no injected current). Consistent with the well-known CA3 origin of SPWs[1,4], firing from CA3c PCs peaked 23.7 ± 9.5 ms before SPWs recorded at the CA1 stratum radiatum (estimated from 5-ms binned histograms, $n = 4$, $P = 0.0074$, $t(3) = -6.4838$, paired $t$ test). CA3c PC firing increased significantly during SPW ripples ($P = 0.0464$, $t(3) = -3.27$; Fig. 6c). In contrast, CA2 PCs ($n = 3$) consistently exhibited firing suppression ($P = 0.0441$, $t(2) = 3.13$, paired $t$ test; Fig. 6c). Depolarized CA1 PCs were sharply activated above their baseline firing level ($n = 6$, $P = 0.0173$, $t(5) = -3.49$, paired $t$ test; Fig. 6c), whereas firing suppression dominated in hyperpolarized CA1 PCs during SPW ripples ($n = 7$, $P = 0.0275$, $t(6) = 2.89$; Fig. 6c). These values are consistent with those reported for extracellular recorded populations of CA3 and CA1 PCs in both drug-free conditions[4] and under urethane[6,28]. Notably, CA1 PC participation during SPW ripples, defined as the proportion of events a cell fired within 60 ms of the SPW peak was significantly higher in depolarized than hyperpolarized cells ($P = 0.0034$, $t(12) = 3.63$; Fig. 6d) and was positively correlated

with the SPW-associated driving force (Fig. 6d). On average, depolarized cells fired more spikes per SPW ripple (0.71 ± 0.43) than hyperpolarized cells (0.04 ± 0.06, $P = 0.0002$, rank sum = 63, Mann-Whitney). In the subset of cells with histological confirmation ($n = 6$ depolarized, $n = 4$ hyperpolarized), SPW ripple participation exhibited a robust tendency along the distance to radiatum (Fig. 6e). Indeed, superficial/CB+ cells had stronger participation than deep/CB− PCs (Fig. 6e). Similarly, the firing rate of CA1 PCs during SPW ripples was correlated with the anatomical differences observed in deep and superficial CA1 sublayers (Fig. 6f).

## CA1 PC participation during SPW ripples in drug-free conditions

Finally, we aimed to confirm our predictions regarding SPW-ripple participation of CA1 PCs across the deep-superficial axis in the drug-free context. To this purpose, we implemented CA1 single-cell recordings with glass pipettes in freely moving rats ($n = 11$ cells; Fig. 7a) using a microdrive that enables mounting and remounting in drug-free conditions[29]. Recordings in an open field during movement and sleep were followed by juxtacellular labeling and *post hoc* histological validation ($n = 6$ cells; Supplementary Table 2 and Supplementary Fig. 7a–c). The action potential waveform and firing autocorrelogram of each cell (Fig. 7b) were used to classify unlabeled cells as PCs on the basis of their similarities to juxtacellularly labeled CA1 PCs. In freely moving rats, CA1 PC participation of SPW ripples is known to be spatially modulated across sleep and wakefulness[20,30,31]. Thus, we analyzed these effects on sleep and awake SPW ripples defined using behavioral and electrophysiological information (Supplementary Fig. 7d–g).

We investigated the effect of behavioral state on SPW ripple participation by identifying events (>10) occurring during sleep and awake conditions in the same rat ($n = 6$ CA1 PCs, 1 histologically confirmed; Fig. 7a,c and Supplementary Table 2). Although no behavioral effect dominated baseline firing ($P = 0.1887$, $t(5) = -1.52$) or the firing rate during SPW ripples events ($P = 0.8661$, $t(5) = -0.18$), we found significantly higher participation of CA1 PCs in awake versus sleep SPW-ripples ($P = 0.0420$, $t(5) = -2.71$; Fig. 7d,e). To account for spatial effects, we evaluated PC firing from rats exhibiting substantial exploratory activity and a sufficient number of SPW ripples recorded during pauses at more than two locations ($n = 6$ cells, 3 histologically confirmed; Fig. 7f–h and Supplementary Table 2). Consistent with the well-known spatial modulation of hippocampal activity, indices of CA1 PC firing exhibited large variability in the recording arena (Fig. 7i). A permutation test for each cell (100 replicates) confirmed substantial spatial bias for the firing rate during SPW ripples in 2 of 6 cells (no bias in the number of SPW events accounted for this effect; Supplementary Table 2). Indeed, the variability of the firing rate during SPW ripple events recorded in the entire session was strongly correlated with the number of visited locations for all cells ($r = 0.71$, $P = 0.0134$; Fig. 7j), confirming that a large part of the variance could be explained by this factor.

Can behavioral state and spatial variability in freely moving conditions still allow for detection of a deep-superficial effect of CA1 PC participation during SPW ripples? SPW ripple participation and firing rate across different states (awake, sleep) and spatial locations of individual PCs did not reveal deep-superficial differences (participation: $r = -0.68$, $P =$

0.312; firing rate: $r = -0.69$, $P = 0.3$; $n = 6$ identified CA1 PCs). However, when sleep and awake SPW ripples were considered together and used as an estimation of overall cell participation and firing rate, we found a significant correlation with PC soma distance to stratum radiatum (SPW-r participation, $P = 0.0423$, $r(6) = -0.82$, Pearson correlation; firing rate during SPW-r, $P = 0.0306$, $r(6) = -0.85$, Pearson correlation; Fig. 7k), similar to the urethane data reported above (Fig. 6e,f). CB immunoreactivity was confirmed in only 4 of 6 cells, preventing us from evaluating the effect of deep/superficial and CB+/CB− classification directly (Fig. 7l,m and Supplementary Table 2). Thus, the variability of CA1 PC firing during SPW ripples recorded in freely moving conditions not only reflects spatial and state-dependent effects[20], but also a deep-superficial gradient of PC participation.

## DISCUSSION

Our data highlight a different participation of deep and superficial PCs during SPW ripples and question the view of hippocampal pyramidal cells as a functionally uniform population during these events. The cell type–specific firing of a variety of morphologically identified hippocampal GABAergic interneurons was initially recognized using extracellular recordings and juxtacellular labeling in urethane-anesthetized rats[6] and was further confirmed in unanesthetized conditions for some interneuronal types[30,32,33]. However, neither single nor multi-electrode recordings have successfully separated PCs during SPW ripples, although differences are evident during theta and gamma oscillations[17,18] and some indications were recently reported[19]. *In vitro*, the variability of PC participation during SPW ripple events has been recognized and associated with different factors[34-36]. Intracellular studies in un-anesthetized rodents did not attempt to differentiate, probably as a result of poor sampling from deep and superficial neurons in relatively unfavorable conditions for long-lasting recordings and labeling[8,9,37,38]. Although these reports highlight consistent SPW-associated intracellular depolarization in CA1 PCs[9], evidence of concurrent somatic inhibition and dendritic excitation suggests that complex intracellular interactions occur[3,5]. Possibly, variability resulting from synaptic fluctuations, together with differences in the number and timing of events, as well anatomical factors, could camouflage potential differences in these studies. Our sharp electrode recording approach under urethane is especially suitable for overcoming some of these limitations, as it allows long-lasting intracellular recordings and unbiased labeling of a variety of CA1 PCs along the deep and superficial sublayers under stable network oscillations.

We found that stronger and more appropriately timed PV-mediated perisomatic inhibition of deep versus superficial cells is one leading determinant of CA1 PCs dynamics. GABAergic inhibition was consistently stronger in deep cells no matter whether it was activated di-synaptically from CA3 or CA2 or directly at perisomatic regions in the presence of glutamate receptor antagonists. Under this last condition, suppression of PV+ basket cell–mediated inhibition with DAMGO occluded group differences. This is consistent with recent reports from paired recordings on preferential connectivity between PV+ basket cells and deep CA1 PCs in mice[16] and with our data on a dominant SPW-associated inhibitory drive close to the $GABA_A$-receptor reversal in deep cells. In contrast, superficial CA1 cells were typically depolarized beyond their resting membrane potential. We found that these cells were preferentially innervated by CCK+ basket cells compared with deep CA1 PCs, but this

connection appeared to be less likely to contribute to deep-to-superficial functional differences than what has been reported in neocortex[39]. In the ventral CA1 region of mice, paired recordings between CCK basket cells and deep/superficial pyramidal cells did not reveal a significant functional difference or a gradient of CB1-immunoreactive boutons[16]. Although species and regional differences may be factors, ultrastructural differences in CB1R and PV somatic boutons[24] and their unitary IPSC dynamics[26] may also contribute[40]. Recent data suggest that CB1 receptor pharmacological modulation of GABA release is not necessarily correlated with CB1 immunolabeling[41], suggesting that unknown signaling mechanisms are in place. PV basket cells and bistratified cells markedly increase their firing during SPW ripples[6,7], whereas CCK+ basket cells do not show a clear relationship and, at least under urethane, poorly participate[6,7]. Instead, GABA release from CCK cells is more likely to contribute during theta oscillations[7,42]. Alternatively, SPW ripple active bistratified cells targeting dendrites could have additional roles in separating deep and superficial PCs.

SPW ripples are a candidate mechanism underlying memory consolidation[31,43]. Participation of CA1 cells during SPW ripples is spatially modulated across brain states[17,20,30,33], but the underlying mechanisms are unknown. During exploratory pauses, neuronal replay of CA1 PCs during awake SPW ripples is location dependent and exhibits a complex interaction with place fields that contribute to firing reactivation during subsequent sleep SPW[20,31]. Our single-cell recordings and juxtacellular labeling in freely moving rats confirmed that CA1 PC participation of SPW ripples is spatially modulated across behavioral states. Notably, in spite of this variability, we successfully confirmed a deep-superficial gradient of CA1 PC participation in drug-free conditions. We speculate that the gradient of the excitatory/inhibitory ratio underlying different driving forces of deep and superficial PCs will modulate the dynamics of replay and consolidation of memory traces during awake and sleeping periods. It is possible that potential long-range projection specificity of deep and superficial CA1 PCs[16] could further amplify the functional effect of their differential activity.

According to our data, the operation of the CA3-CA1 microcircuit during SPW ripples was controlled by an appropriately timed gear assembly of interactions (Supplementary Fig. 8). Firing increases by CA3 PCs quickly propagated to activate their downstream targets at CA2 and CA1. Firing suppression of CA2 PCs caused by strong di-synaptic inhibition[27,44,45] releases deep CA1 PCs from a dominant excitatory action[15], which, together with firing from PV+ basket cells[6,7,32], results in a major inhibitory drive during SPW ripple events. In contrast, superficial CA1 PCs are preferentially innervated by CCK+ basket cells, which fire less consistently than PV+ basket cells during these events[7], leaving them under the dominant control of CA3 PC firing, as reflected in driving force and reversal potential values. SPW ripple active interneurons, such as PV+ basket cells and bistratified cells, may enable the phasic firing of active pyramidal cells during ripple cycles (for example, for the correct temporal order of a reactivated ensemble). The spatiotemporal specialization of hippocampal microcircuits is therefore far more complex than originally thought[6,46].

Although SPW-ripples are the more synchronous event recorded in the healthy hippocampus, their role in neurological disease is less well understood. In temporal lobe epilepsy, pathological high-frequency ripple-like oscillations are conspicuously related to

epileptogenic regions, but their relationship with physiological ripples is questioned[47,48]. Ambiguity on the intracellular correlates of extracellular ripples, whether physiological- or pathological-like, are already recognized[36,49] and suggest that more work is required to fully understand the generators of these events. Different vulnerabilities of deep and superficial CA1 PCs to anoxia and seizures are a common feature[50]. Our data regarding a disparate correlation of deep and superficial cells with the SPW and the ripple components opens the door to new interpretations of the major cellular contributors to the SPW-ripple complex in health and disease.

## ONLINE METHODS

All experimental protocols and procedures were performed according to the Spanish legislation (R.D. 1201/2005 and L.32/2007), the European Communities Council Directives of 1986 (86/609/EEC) and 2003 (2003/65/CE) for animal research, and were approved by the Ethics Committee of the Instituto Cajal (CSIC). Single-cell recordings in freely moving rats were obtained in both Madrid and at the University of Szeged, Hungary. Those experiments in Hungary were approved by Animal Care Committee of the University of Szeged.

### *In vivo* electrophysiology under urethane anesthesia

Males and female Wistar rats (250–450 gr) were anesthetized with urethane (1.2 g per kg of body weight, intraperitoneal) and fastened to the stereotaxic frame. Body temperature was kept constant at 37°. Two bilateral craniotomies of ~1 mm diameter were performed above both hippocampi for CA3 stimulation (AP: −1.2 mm, ML: 2.9 mm), and a window of ~2 mm diameter was drilled above the right hippocampus for CA1, CA2 and CA3 recordings (AP: −3.7 mm; ML: 3 mm). The dura was gently removed to allow electrode penetration. To decrease brain pulsations the cisterna magna was opened and drained.

Two concentric bipolar stimulating electrodes were advanced 3.5 mm with 30° in the coronal plane to target CA3. Stimulation consisted of biphasic square pulses of 0.2-ms duration and amplitudes of 0.050–1.2 mA every 5 s. A subcutaneous Ag/AgCl wire was placed in the neck as a reference electrode.

A 16-channel linear silicon probe (NeuroNexus Tech; 100-μm interspaced contact) was advanced perpendicular along the CA1-DG-CA3c axis guided by extracellular stimulation and typical electrophysiological hallmarks including: (i) multi-unit activity from the CA1 and CA3 stratum pyramidale and the granule cell layer of the dentate gyrus, (ii) spontaneous ripple events to identify CA1 cell layer with the associated sharp-wave events to identify the stratum radiatum, and (iii) the spatial distribution of theta oscillations (4–12 Hz) and gamma activity (20–90 Hz). Extracellular signals were pre-amplified (4× gain) and recorded with a 16(32)-channel AC amplifier (Multichannel Systems), further amplified by 100, filtered by analog means at 1 Hz to 5 kHz, and sampled at 20 kHz per channel with 12 bits precision using a Digidata 1440 (only 14 channels were stored to allow for simultaneous recording with intracellular current and voltage signals). Recording and stimulus position was confirmed by post-hoc histological analysis of the tracks (see below).

For intracellular recording and labeling, sharp pipettes were pulled from 1.5 mm/0.86 mm outer/inner diameter borosilicate glass (A-M Systems) on a Flaming-Brown puller (Sutter Instruments) and filled with 1.5 M potassium acetate and 2% Neurobiotin (wt/vol, Vector Labs). *In vivo* pipette impedances varied from 50–100 MΩ. Intracellular recordings were obtained blindly, driven by a hydraulic manipulator (Narishige) and guided by extracellular stimulation (Supplementary Fig. 1a). Signals were acquired with an intracellular amplifier (Axoclamp 900A) at 100× gain. Before recordings started, the craniotomy was covered by 3% agar to improve stability. Passive and evoked physiological properties were recorded in current-clamp mode in CA1 ($n = 25$), CA2 ($n = 3$) and CA3c ($n = 4$) cells. The resting potential, input resistance and amplitude of action potentials was monitored all over the course of experiments. After data collection, Neurobiotin was ejected using 500-ms depolarizing pulses at 1–3 nA at 1 Hz for 10–45 min. The electrode was then gently retracted while monitoring cell survival and the final offset (Supplementary Fig. 1a). Pyramidal cell identity was first inferred by electrophysiological criteria—spontaneous activity, action potential waveform, firing response to depolarizing current pulses and CA3 antidromic/orthodromic response—and subsequently confirmed by morphological analysis (Supplementary Fig. 1a). Pyramidal cells included in this study had stable resting potentials of at least −40 mV and access resistances lower than 20 MΩ.

### *In vivo* pharmacology under urethane anesthesia

For pharmacological manipulations *in vivo*, we used an 8-channel linear probe with a fluidic tube mounted on the tip (D-series, NeuroNexus Tech). Between 1–2 μl of a cocktail containing the glutamate receptor antagonists CNQX/AP5 (3mM/30 mM) and the Texas Red conjugated dextran tracer (0.1 mg $ml^{-1}$; Molecular Probes) in artificial cerebrospinal fluid (ACSF, in mM: 124 NaCl, 5 KCl, 1.5 $MgSO_4$, 26 $NaHCO_3$, 3 CaCl2, 10 glucose, pH 7.3; bubbled with 95% $O_2$/5% $CO_2$,) was slowly (~0.1 μl $min^{-1}$) delivered using a Hamilton syringe coupled to the fluidic cannula by an oxygen-impermeable Tygon tube (R-3603; Cole-Parmer). After completing experiments ($n = 2$ rats), brains were fixed (see below) to analyze the reach of drug infusion (Supplementary Fig. 1c–e).

### *In vitro* electrophysiology

Juvenile (P15–25, $n = 38$) and adults (P39–58; $n = 5$) male and female Wistar rats were used to prepare hippocampal slices. Animals were anesthetized with ketamine-xylazine (100 mg/kg, 10 mg/kg) and decapitated using approved procedures. Sagittal slices (400 μm) were prepared from the septal level of the hippocampus at 2–4 mm from midline using a Leica vibratome (Leica VT1200S). The composition of the extracellular solution (ACSF) was (in mM): 125 NaCl, 4.25 KCl, 3 $CaCl_2$, 1 $MgCl_2$, 22 $NaHCO_3$, 1.2 $NaH_2PO_4$, 10 glucose, pH 7.3 when balanced with 95% $O_2$/5% $CO_2$. Slices recovered in an interface chamber for at least 1 h at 22–25 °C in ACSF. For recordings, one slice was transferred each time from the storaging to the submerged recording chamber. A peristaltic pump (Gilson) was used to uniformly circulate the ACSF (2.5–3 ml $min^{-1}$) through the recording chamber using oxygen-impermeable Tygon tubes. Somatic patch-clamp recordings were made from CA1 pyramidal cells under visual control with an upright microscope (BX51W, 60× lens; Olympus) at 32 °C, using patch pipettes (pulled from borosilicate glass capillaries; Harvard Apparatus) and filled with (in mM): 40 cesium gluconate, 90 potassium gluconate, 3 KCl,

1.8 NaCl, 1.7 $MgCl_2$, 1 EGTA, 10 HEPES, 2 $K_2ATP$, 0.3 NaGTP, 10 mM phosphocreatine and 0.025% Alexa568, pH 7.3 adjusted with KOH (osmolarity ~300 mOsm). Using cesium gluconate solutions facilitated voltage-clamp recordings but prevented appropriate characterization of firing patterns in current-clamp mode. Electrodes filled with this solution had resistances of ~7 MΩ.

A bipolar stimulating electrode (tungsten wires, 0.5-mm separation, 0.5 MΩ) were positioned under visual control at the stratum pyramidale of either CA3 (Fig. 5a), CA2 (Fig. 5j) or CA1 (for evaluating perisomatic inhibition; Fig. 5h). For extracellular field potential recordings at the CA1 stratum radiatum, we used a patch-clamp pipette filled with ACSF coupled to one-channel AC amplifier (DAM-80; WPI). Patch recordings were performed using the whole-cell configuration in current- and voltage-clamp modes with an Axoclamp 2B amplifier (Molecular Devices) and digitized with a Digidata 1440A (Molecular Devices) at a sampling frequency of 20 kHz. Capacitance compensation and bridge balance were performed for current-clamp recordings. The junction potential (~15 mV) was not corrected.

Drugs used include: 6-cyano-7nitro-quinoxaline-2,3-dione (CNQX, 10-20 μM, Sigma-Aldrich) and D-2-amino-5-phosphonopentanoate (AP5, 50 μM, Sigma-Aldrich), [S-(R*,R*)]-[3-[[1-(3,4-dichlorophenyl)ethyl] amino]-2-hydroxypropyl] (cyclohexylmethyl) phosphinic acid (CGP54626, 1 μM, Tocris Bioscience), [D-Ala2,N-MePhe4,Gly-ol5] enkephalin (DAMGO, 100-200 nM, Tocris Bioscience), R-(+)-(2,3-dihydro-5-methyl-3-[(4-morpholinyl)methyl]pyrol[1,2,3-de]-1,4-benzoxazin-6-yl)(1-naphthalenyl)meth anone mesylate (WIN55,212, 5 μM, Sigma-Aldrich).

### Single-cell recordings and juxtacellular labeling in drug-free freely moving rats

Single-cell recordings followed by juxtacellular labeling for *post hoc* immunohistochemical identification were obtained from freely moving rats during awake resting periods or during sleep using a miniature microdrive adapted to house glass electrodes[29]. Both male and female Wistar rats (300–450 g) were implanted with the microdrive holder consisting of a plastic base with a cylindrical hole (2.5 mm) targeting a small craniotomy (4.3 mm posterior to Bregma and 2.5 mm lateral) under isoflurane anesthesia (1.5–2% mixed in oxygen 400–800 ml $min^{-1}$). The dura mater was left intact. The craniotomy was cleaned with 0.05–0.07 mg $ml^{-1}$ Mitomycin C (Sigma) to reduce growth-tissue, filled with agar (2.5–3.5%) and covered to avoid drying. A ground epidural platinum/iridium wire (125 μm) was implanted over the cerebellum and used as reference.

To habituate animals to microdrive mounting/remounting in awake and drug-free conditions, craniotomy cleaning was repeated over 4–5 consecutive days after surgery. Animals were habituated daily to the recording arena (40 × 40 × 23 cm or 25 × 25 × 35 cm) and microdrive-holder manipulations with water and food ad libitum. Only data from the 40 × 40 × 23 cm arena were used for spatial analysis (see below). Recordings were obtained over the light cycle (12-h light/dark cycle). The day of recording, the microdrive housing a glass pipette (1.0 mm × 0.58 mm, ref 601000; A-M Systems) filled with 1.5–2.5% Neurobiotin in 0.5 M NaCl (impedance 8–15 MΩ) was mounted in the holder and gently advanced into the animal's brain (350 μm per revolution at 3–5-μm resolution). In two animals, an ipsilateral cortical EEG screw over the prefrontal cortex and a contralateral intrahippocampal tungsten

wire (122 μm) targeting the stratum radiatum were implanted for validating definition of behavioral states. Recordings were obtained with a miniature pre-amplifier (ELC mini-preamplifier, NPI Electronic, Germany), carrying two LEDs, and customized to connect with an Axoclamp-2B amplifier (Molecular Devices). In some animals a microdrive adapted for housing an independent sharpened tungsten-wire electrode for LFP recording was used (100–400-μm separation between pipette and wire). A video-camera was used to monitor the animals' behavior (sleep, awake, movement) and to track their position in the recording arena. Images were acquired at 27 frames per s. The depth position of the pipette was inferred from the micrometric scale of the microdrive[29] and from the shape of relevant LFP signals, including K-complexes with spindles while going through the cortex and hippocampal SPW-ripples. Single CA1 pyramidal cells were randomly targeted at the dorsal hippocampus following both stereotaxic and extracellular waveform criteria. After recording, cells were modulated using the juxtacellular labeling technique with positive current pulses (500–600-ms on-off pulses; 5–18 nA) while monitoring their response as previously reported[51]. After experiments, rats were perfused with 4% paraformaldehyde (wt/vol) and the brain cut in 70-μm coronal sections. Labeled CA1 pyramidal cells were identified using streptavidin-conjugated fluorophores.

### Tissue processing and immunohistochemistry

For *in vivo* experiments, 1–2 h after completing recordings rats were transcardially perfused with 4% paraformaldehyde (PFA) and 15% saturated picric acid (wt/vol) in 0.1 M, pH 7.4 phosphate-buffered saline (PBS). In initial experiments, picric acid was not included. Brains were postfixed overnight at 22–25 °C, washed in PBS and serially cut in 70-μm coronal sections (Leica VT 1000S vibratome). Rats selected for synaptic bouton counting ($n = 3$) were perfuse-fixated with 4% PFA, 15% saturated picric acid and 0.05% glutaraldehyde (vol/vol) in 0.1 M phosphate buffer, without further post-fixation. Sections containing the stimulus and probe tracks were identified with a stereomicroscope (S8APO, Leica). Sections containing Neurobiotin-labeled cells were localized by incubating them in 1:400 Alexa Fluor488–conjugated streptavidin (Jackson ImmunoResearch 016-540-084) with 0.5% Triton X-100 (vol/vol) in PBS (PBS-Tx) for 2 h at 22–25 °C. After three washes, sections were analyzed in an inverted epifluorescence microscope (Leica, DMI6000B). Those containing the recorded soma were selected for immunofluorescence characterization (Supplementary Fig. 1a), and several adjacent sections were used for synaptic bouton studies in $n = 2$ identified cells (Supplementary Fig. 5). For *in vitro* experiments, recorded sagittal slices (400 μm) were fixed by immersion in 4% PFA in PBS overnight at 22–25 °C, and washed three times in PBS before immunofluorescence labeling.

Sections with either *in vivo* or *in vitro* recorded cells were equally processed, except for the Tx concentration in solutions and washes: 0.5% for *in vivo*, and 1% for *in vitro*. They were blocked with 10% fetal bovine serum (FBS, vol/vol) in PBS-Tx and incubated overnight at 22–25 °C with the primary antibody solution containing rabbit anti-CB (1:1,000, CB D-28k, Swant CB-38), or mouse anti-CB (1:1,000, CB D-28k, Swant 300) and rabbit anti-PCP4 (1:300, Sigma HPA005792), with 1% FBS in PBS-Tx. After three washes in PBS-Tx, sections were incubated for 2 h at 22–25 °C with appropriate secondary antibodies: goat anti-rabbit Alexa Fluor633 (1:500, Molecular Probes, A21070), and goat anti-mouse Alexa

Fluor488 (Jackson Immunoresearch 115-545-003) or goat anti-mouse Rhodamine Red (1:200, Jackson ImmunoResearch, 115-295-003) in PBS-Tx-1%FBS. Following 10-min incubation with bisbenzimide H33258 (1:10,000 in PBS, Sigma, B2883) for nuclei labeling, sections were washed and mounted on glass slides in Mowiol (17% polyvinyl alcohol 4-88 (wt/vol), 33% glycerin (vol/vol) and 2% thimerosal (vol/vol) in PBS).

To analyze synaptic boutons with immunohistochemistry, sections were blocked with 20% normal horse serum (NHS, vol/vol) in Tris-buffered saline with 0.3% Triton X-100 (TBSTX), followed by primary antibody incubation in 1% NHS in TBSTX for at least 3 days at 4 °C. After washing 3× 10 min in TBSTX, sections were incubated with secondary antibodies in 1% NHS in TBSTX overnight at 4 °C. Sections were washed 3× 10 min in TBSTX and mounted to glass slides in VectaShield (Vector Laboratories). The primary antibodies used in this case were: Mouse anti-gephyrin (1:500, Synaptic Systems, 147 011), goat anti-parvalbumin (1:1,000, Swant, PVG-214), guinea pig anti-CB1R (1:1,000, Frontier Institute, Hokkaido, Japan CB1-GP-Af530), rabbit anti-Wfs-1 (1:500, Proteintech. 11558-1-AP). The following secondary antibodies were used (all raised in donkey): anti-mouse or anti-rabbit DyLight405 (1:250 and 1:400, Jackson ImmunoResearch; 715-475-151 and 711-475-152, respectively), anti-mouse, anti-goat, anti-guinea pig Alexa Fluor 488 (1:400, Jackson ImmunoResearch Laboratories; 715-546-150, 705-546-147 and 706485148, respectively); anti-goat and donkey anti-guinea pig Cy3 (1:400, Jackson ImmunoResearch; 705-165-147 and 706-165-148, respectively); and anti-rabbit, anti-goat or anti-guinea pig Cy5 (1:400; Jackson ImmunoResearch; 711-175-152, 705-175-147 or 706-175-148, respectively). For processing gephyrin in recorded cells (Supplementary Fig. 5), we implemented antigen retrieval protocols. Negative controls lacking the primary antibodies were always included.

## Antibodies

Specificity information for primary antibodies: CB, rabbit polyclonal produced by immunization with recombinant rat CB D-28k, antiserum; characterized in rat[52]; no signal in mouse knockout[53]. CB, mouse monoclonal from chicken CB D-28k, hybridoma supernatant; generated and characterized previously[54]; similar immunoreactivity as for the rabbit antibody. PCP4 (Purkinje cell protein 4), rabbit polyclonal from 6–58 aa of recombinant human PCP4, similar immunoreactivity as for another PCP4 antibody used previously[55]. Gephyrin, mouse monoclonal from N-terminal of rat gephyrin, 100 μg $ml^{-1}$; purified IgG, generated previously[56]; no Geph7a signal in mouse knockout[57]. Parvalbumin, goat polyclonal from rat parvalbumin, antiserum; similar immunoreactivity as for other parvalbumin antibodies[52]; no signal in mouse knockout[58]. CB1R (cannabinoid receptor 1), guinea pig polyclonal from C-terminal 31 aa of mouse CB1R, 200 μg/ml; similar immunoreactivity as for other CB1R antibodies, western blot single band at 52 kDa[59]. Wfs1 (Wolfram syndrome 1), rabbit polyclonal from fusion protein 1–314 aa of recombinant human Wfs1, 280 μg $ml^{-1}$; immunoreactivity in rat brain and molecular weight (~100 kDa) similar to rabbit anti-WFS1C antibody[60].

## Confocal imaging

To acquire multichannel fluorescence stacks from recorded cells, a confocal microscope (Leica SP5) with LAS AF software v2.6.0 build 7266 (Leica) was used. For single-cell studies the following channels (fluorophore, laser and excitation wavelength, emission spectral filter) were used: i) bisbenzimide, Diode 405 nm, 415–485 nm; ii) Alexa Fluor488, Argon 488 nm, 499–535 nm; iii) Rhodamine Red/Alexa Fluor568/Texas Red, DPSS 561nm, 571–620 nm; iv) Alexa Fluor633, HeNe 633 nm, 652–738 nm; and objectives HC PL APO CS 10.0×0.40 DRY UV, HCX PL APO lambda blue 20.0×0.70 IMM UV and HCX PL APO CS 40.0×1.25 OIL UV.

For bouton counting experiments, as well as for documenting two CA1 pyramidal cells (see Supplementary Fig. 5), an LSM710 confocal microscope (Axio Imager Z1, Zeiss) with ZEN 2008 software v5.0 (Zeiss) was used, with the following channels (fluorophore, laser excitation wavelength, emission band): i) DyLight405, 405 nm, 409–499 nm; ii) Alexa Fluor 488, 488 nm, 493–542 nm; Cy3, 543 nm, 552–639 nm; iii) Cy5, 633 nm, 637–757 nm; and a DIC M27 Plan-Apochromat 63×/1.4 n.a. oil immersion objective lens. Channels were acquired sequentially with an 8-bit dynamic range, with a pinhole of 1 Airy unit typically for the shortest wavelength; the pinhole sizes of the other channels were adjusted to give the same optical slice thickness. With the 405 nm laser, the optical slice thickness was typically 0.6 μm; with the 488-nm laser 1 Airy unit gave an optical slice thickness of 0.7 μm. With the 405-nm laser, sampling resolution was typically 12.7 pixel $\mu m^{-1}$, 0.08 × 0.08 × 0.43 μm voxels

Assignment of antibody fluorophores was based on minimizing spectral overlap between channels.

## DAB processing of *in vivo* recorded cells

After completing confocal studies, sections with Neurobiotin-labeled neurons were demounted from slides and together with all remaining sections were rinsed in PBS-0.5%Tx and treated with 0.3% $H_2O_2$ (vol/vol) for peroxidase inactivation. After further washes, they were incubated with 1% B solution (biotinylated peroxidase complex, vol/vol) of the ABC kit (Vectastain ABC Elite kit, Vector Laboratories, PK6100) in PBS-Tx-2%FBS for 4 h at 22–25 °C, and afterwards with 1% A/1% B kit solutions in PBS-Tx-FBS for 3 d at 4 °C. Following three washes, slices were processed with diaminobenzidine (DAB, Sigma) using the glucose oxidase method, with or without nickel intensification: 0.05% DAB (wt/vol), 0.2% glucose (wt/vol), 0.004% ClNH4 (wt/vol), 0.04% $Ni(NH_4)_2)SO_4)_2$ (wt/vol) and 0.002% glucose oxidase (wt/vol) in PBS. Reaction was observed at a stereomicroscope and stopped by several rinses in PBS. Sections were then mounted in slides, dehydrated (in ethanol 70–95%-100% and xilol) and coverslipped with DPX (VWR). Subsequently, labeled cells were examined and photographed in a bright-field microscope (Nikon Eclipse 80i) coupled to a digital camera (Mbf). Two-dimensional reconstructions were made with a drawing camera lucida tube (Fig. 3a).

### Morphological data analysis

All morphological analyses were performed blindly to electrophysiological data. Assignment of cell location (Fig. 3b) and probe track position (Fig. 1b) was based on anatomical landmarks[61]; the mediolateral coordinate was directly measured from the midline. The orthogonal distance from the recorded cell to the probe track (Fig. 2f) was estimated by triangulation using previous measurements. The distance from the cell soma to radiatum (Fig. 3b) was measured from camera lucida drawings (1 section of 70 μm at 40×). The lineal distance from the cell soma to CA2 was taken parallel to the stratum pyramidale in the same section. The border between CA1 and CA2 was defined at the end of the stratum lucidum.

For stereological quantification of gephyrin-immunopositive puncta (Fig. 4), we selected Wfs1-positive CA1 pyramidal cells ($n = 34$) in 4 sections (4 confocal stacks) obtained from 3 different rats. We counted all gephyrin/PV and gephyrin/CB1R boutons from 11 optical slices around the soma center, using the first image in the stack as a lookup section for the optical dissector. The sampling area was calculated from the product of the mean circumference of the soma and the 10 optical slices. The border with radiatum was estimated for each section and the distance from the cell somata were measured using ImageJ.

For evaluation of CB immunoreactivity (Supplementary Table 1) in the CA1 stratum pyramidale, we adopted a quantitative approach (details in Supplementary Fig. 4). Briefly, for each confocal image containing the soma of a recorded identified neuron, we measured the mean pixel intensity of the CB signal (Alexa Fluor633 immunofluorescence) both from the recorded cell and from neighboring pyramidal cells in the same optical section by drawing conversative ROIs around their somata (avoiding CB+ axons and dendrites) in ImageJ. Some cells were intensely immunopositive (CB+) and others were immunonegative (CB−). We defined CB intensity of the recorded cell as a normalized intensity value (Supplementary Fig. 4b). A binary classification of CB+ and CB− pyramidal cells was adopted, with immunonegative cells classified as CB− (normalized intensity threshold <0.2) and neurons with intense (normalized intensity >0.75) or intermediate immunoreactivity to CB classified as CB+ (Supplementary Figs. 3c–e and 4). To classify cells as deep and superficial pyramidal cells (Fig. 5d), we considered the positions of the soma with respect to the more compact CB sublayer. Cells were defined as “deep” if identified somata were located away from the CB positive sublayer, independent of their immunoreactivity to CB; “superficial” cells were defined as having their soma within the CB positive sublayer. For *in vitro* studies at P15 to P58 cells were classified similarly. Only slices with clear CB expression at the recorded coordinate were included in the database, to circumvent a late developmental onset of CB expression. Calbindin quantification was evaluated independently in a subset of cells by two authors (EC and TJV) who reached to comparable measurements.

All confocal images were processed in ImageJ/Fiji (v1.49b)[62] and Adobe Photoshop CS5 Extended (v12.0.4x64). Colocalization between markers (channels; for example, Fig. 4b,c) was evaluated in the same optical section.

### *In vivo* data analysis

Data analysis was performed using routines written in MATLAB 7.10 (MathWorks). Electrophysiological properties (input resistance, membrane capacitance and membrane time constant) of neurons recorded intracellularly *in vivo* were measured using 500-ms currents step in current-clamp mode (Supplementary Table 1). In single-cell recordings with glass pipettes in freely moving rats, we evaluated the stability of the action potential waveform (peak-to-peak duration and amplitude as well as a spike asymmetry index defined as the ratio of the difference between the negative and positive baseline-to-peak amplitudes and their sum) over the entire recording session (minimum 3 min), before juxtacellular electroporation. To evaluate firing features typical of PCs an autocorrelogram of the single-cell firing rate was estimated (0.5-ms bins). CA1 PC usually fire complex-spike bursts with autocorrelogram peaks at 4–5 ms (Fig. 7b and Supplementary Table 2). Cells with intracellular action potential amplitude smaller than 40 mV were excluded. Single-cell drug-free recordings with action potentials wider than 1 ms and large amplitude variability over the recorded session were excluded from the analysis.

Electrophysiological analyses were performed with the whole database at once. Groups (depolarized/hyperpolarized, deep/superficial, CB+/CB−) were identified using criteria that are specified along the text.

Local field potential (LFP) recordings from sites at the stratum radiatum were low-pass filtered at 100 Hz to study SPWs. LFP signals from sites at the stratum pyramidale were bandpass filtered between 100–600 Hz to study ripples. We used forward-backward-zero-phase finite impulse response (FIR) filters of order 512 to preserve temporal relationships between channels and signals. For SPWs, filtered signals were smoothed by a Gaussian kernel and candidate events were detected by thresholding (>3 s.d.). For ripple detection, the bandpass-filtered signal was subsequently smoothed using a Savitzky-Golay (polynomial) filter and candidate events were detected by thresholding (>2 s.d.). Only SPW events associated to stratum pyramidale ripples were included for analysis. All pairs of detected events were visually confirmed and aligned by the peak of the accompanying individual SPW (or by the local maximum of the smoothed ripple). One-dimensional current-source density (CSD) signals were calculated from the second spatial derivative of LFP and treated similarly for SPW detection. Smoothing was only applied to CSD signals for visualization purposes. Tissue conductivity was considered isotropic, and an arbitrary value of 1 was assigned to express CSD signal as $mV/mm^2$. Stripes in the background CSD due impedance and offset differences between sites were clearly separated from the relevant CSD responses. For both LFP and CSD signals, data were represented as averages of 10–112 individual events.

For analysis of SPW-associated intracellular responses (Fig. 1c,d), the timing of SPW-ripple events was used to align membrane potentials at different levels. We found similar intracellular trends when the peak of the SPW or the ripple power was used for alignment. Evoked responses were aligned by the stimulation trigger (artifact) and input/output curves (Fig. 1e) were obtained for a range of stimulation intensities (50–500 μA). The resting membrane potential (RMP) and input resistance were estimated by linear regression between baseline potential data and the associated holding current. The reversal potential ( $V_{rev}$) of

SPW-associated and evoked responses for each cell was estimated by linear regression between the response peak amplitude and membrane potential (Fig. 1c,d). The driving force of SPW-associated and evoked responses (Fig. 1g) was estimated as $V_{rev}$-RMP.

Time-frequency analysis of intracellular and extracellular ripples (Fig. 2) was performed by applying the multitaper spectral estimation in sliding windows with 97.7% overlap and frequency resolution of 10 Hz in the 90–600-Hz frequency range (only the 90–400-Hz range is shown) to data sweeps aligned by SPW-ripple events (±1 s). The normalized power in the whole time windows was then treated as a statistical distribution, from which we extracted the mode to estimate the oscillatory frequency peak and the mean power spectral value. The ripple power both for intracellular and extracellular signals (Fig. 2e) was estimated from the area within the 90–200-Hz band. To quantify the coordination between the intracellular and extracellular ripple (Fig. 2), we estimated the cross-correlation function between signals for each sweep and calculated the power spectrum of cross-correlation (Supplementary Fig. 3b).

Peri-event time histograms of intracellularly recorded cells (PETHs; Fig. 6c) were obtained by binning (30 ms) action potential timing recorded in the absence of holding currents, i.e. at their resting membrane potential. Individual action potentials were identified by thresholding at mean amplitude. Only isolated SWP-ripples events (on a time windows >1 s) were used to compute PETHs and a minimum number of events (>10) per cell was required. This resulted in a subset of cells that satisfied all conditions. A grand-average of the mean PETHs was calculated pooling individual PETHs in a given cell group. We also evaluated whether cell responses during SPW-ripples (±60 ms around the SPW peak) was different from the baseline firing occurring between 500 and 100 ms before the event (Fig. 6c). We tested different windows lengths (20, 40, 60, 100 ms) and found ±60 ms to better capture statistical differences, consistent with the typical SWP-ripple duration (~50–70 ms).

To evaluate single PC entrainment by SPW ripples (Fig. 6d–f), we defined the following measures: i) cell participation, as the number of events the cell fire over the total number of events (0.1 means the cell fires in 10% of SPW-ripples); ii) the average number of spikes emitted in a 60 ms centered in the SPW-ripple evens, defined from the total count for all events examined; iii) the SPW-associated firing rate in Hz, which is calculated from the average number of spikes in the 60-ms window.

For single-cell recordings in freely moving conditions (Fig. 7), data from glass pipettes were: i) band pass filtered at 100–600 Hz and smoothed using a Savitzky-Golay (polynomial) filter to detect ripple events by thresholding (>4 s.d.); ii) high-pass filtered at 300 Hz to detect positive spikes from the juxtacellular recorded cell (>8 s.d.) (see Fig. 7c). For visualization of ripple events signals were filtered signals at 100–200 Hz. We used forward-backward-zero-phase finite impulse response filters (order 512) to preserve temporal relationships between channels and signals. All events/spikes were visually confirmed. Candidate SPW ripple events were all aligned by the local maximum of the smoothed ripple. In those cases where a second electrode was available for LFP recordings, signals were treated similarly and SPW-ripple events were all validated. PETHs and entrainment by SPW ripples of single-cells recorded in freely moving conditions were

obtained as previously described for intracellular recordings under urethane. Data in different behavioral brain states (sleep and awake) were analyzed separately.

To define the different brain states in freely moving rat experiments we adopted an integrated behavioral and electrophysiological approach. Sleep and awake states were visualized from the videos by two independent researchers (M.V., D.G.-D.) one blind to electrophysiological data. We used written information recorded along the experiments (by R.G.A. and M.V.) and simultaneous LFP activity at the glass pipette to roughly identify epochs of sleep and wakefulness in the same animal ($n$ = 6 out of 11 rats). Definition of brain states in these animals was subsequently refined using specific behavioral and electrophysiological criteria. Under light conditions, rat's sleep is characterized by a curled-up posture typically at a preferred corner of the cage with eyes closed[63]. Hence, sleep was behaviorally defined by the curled immobile posture of the animal at the corner (Fig. 7a), typically associated with slow-wave activity (<3 Hz high amplitude LFP). On occasions, phasic movements typical of paradoxical REM sleep were observed accompanied by low amplitude rhythmic activity at the theta band in the hippocampal LFP (4–12 Hz). Awake states were defined whenever the animals had their eyes open[63] and were attentive either moving or not (Fig. 7b). Animal's position in the arena was tracked using idTracker to account for head movements[64] and/or manually checked in cases of poor contrast. We validated these approaches in two animals carrying an ipsilateral cortical screw for EEG recordings and a contralateral intrahippocampal wire for LFP recordings at the stratum radiatum in addition to the glass pipette (Supplementary Fig. 7). All these signals were recorded together with signals from an accelerometer integrated in the pre-amplifier headstage. Labeled epochs were subsequently used to classify SPW-ripple events as occurring during slow-wave sleep (sleep SPW ripples) or in awake conditions (awake SPW ripples).

To account for the spatial modulation of single-cell firing, we first identified rats exhibiting exploratory activity along several locations (4 × 4) in the 40 × 40 cm arena (>2 locations) and sufficient number of SPW-ripple events detected at each location (>10; $n$ = 6 of 11 rats). The baseline firing rate, the number of SPW-ripples, as well as single-cell participation and firing rate during SPW-ripples were evaluated in the 4 × 4 spatial grid (Fig. 7i). To quantify the spatial modulation of the single-cell firing rate and participation during SPW-ripples for each cell we calculated the s.d. of the spatial index across 4 × 4 locations. Then we performed a Fisher-Pitman permutation test for each cell and index, consisting in randomly shuffling the event location (100 replicates) and testing for significant difference between the observed value and the random distribution. We also tested similarly whether the number of SPW-ripple events had a spatially biased distribution. For the basal firing rate, we proceeded similarly but randomly permuting the animal's position (that is, xy vector). Finally, to account for the spatial effects on the variance of the single-cell participation and firing rate during SPW-ripples we estimated the coefficient of variation of the mean (s.d./mean) for the whole session as a function of the number of visited locations for all cells examined ($n$ = 11).

### Code availability

Routines and codes written in MATLAB 7.10 (MathWorks) are available on request

### *In vitro* data analysis

*In vitro* data was analyzed using tools from pClamp 10.2 (Molecular Devices) and Origin 8.5 (OriginLab). Basic membrane properties (input resistance, membrane capacitance and membrane time constant; Supplementary Fig. 6a) were measured at −60 mV in response to a −20-pA current pulse (300-ms duration).

Evoked EPSC and IPSC amplitudes were measured as the peak current with the cell held at −70, −50 and +10 mV. Amplitude data was correlated with the cell distance to radiatum as estimated by posterior morphological analysis. The onset was measured as the delay from the beginning of the stimulation artifact to the start of postsynaptic response (Supplementary Fig. 6d).

### Statistical analysis and comparisons

Cells from different hippocampal regions were collected randomly and assigned to different groups according to the following criteria: i) CA1, CA2 and CA3 PCs were classified according to anatomical information and neurochemical profiling; ii) depolarized and hyperpolarized CA1 PCs were classified according to their subthreshold membrane response during SPW events recorded intracellularly at the resting membrane potential in urethane; iii) deep and superficial CA1 PCs were classified according to their somatic position regarding to the CB-positive sublayer (the center of the soma within the CB immunoreactive cell band was considered superficial; deep above the CB band); iv) CB-positive or CB-negative was determined by quantitative analysis of CB immunoreactivity (see Supplementary Fig. 4); v) single-cells recorded with glass electrodes in freely moving rats were classified as CA1 PCs based on similarities of their action potential waveform and firing autocorrelogram to those obtained from histologically confirmed CA1 PCs. Given the low sample size (only 4 cells tested for CB out of 6) we did not attempt to classify them as deep/superficial or CB+/CB−.

Group results are given as mean ± s.d., with individual data plotted in each case. No statistical methods were used to predetermine sample sizes, but our sample sizes are similar to those reported in previous publications[36,45]. Statistical analysis was performed using MATLAB or SPSS 17.0. Data were analyzed using two-ways ANOVA, repeated measures ANOVA, Pearson correlation and Student's *t* test (paired or unpaired) considering $P < 0.05$ as statistically significant. All *post hoc* tests are two-tailed. Histograms distribution of several values (SPW-associated reversal potential, driving force, cell participation and firing rate) measured across the entire population of cells was fitted to a Gaussian distribution for cells classified as superficial/deep or CB+/CB− using the Shapiro-Wilk test. Non-parametric tests (Mann-Whitney) were used whenever required.

## Supplementary Material

Refer to Web version on PubMed Central for supplementary material.

## ACKNOWLEDGMENTS

We thank P. Somogyi for his valuable guidance and suggestions on histological procedures and analyses. For gephyrin counting, B. Micklem advised on stereological approaches and K. Wagner helped with tissue processing. We thank B. Gal for histological processing for immunofluorescence studies and F. Laurent for suggestions for analysis. R. Miles, A. Gulyás and A. Colino provided useful comments and discussion. We also thank G. Tamás and V. Szemenyei for their generous support. This work was supported by a grant from the Spanish Ministerio de Economía y Competitividad (BFU2012-37156-C03-01). E.C. receives funding from the CSIC JAE Program, co-funded by the European Social Fund. M.V. was supported by the Spanish Ministry of Education, Culture and Sports (FPU12/03776) and by a short-term grant to visit the MRC Anatomical Neuropharmacological Unit in Oxford (FPU-EST13/01046). A.S.-A. is funded by the Universidad Complutense de Madrid. T.J.V. was supported by the UK Medical Research Council. R.G.A. was supported by an ERC Advanced grant (INTERIMPACT) to G. Tamás. D.G.-D. is funded by the Spanish Ministerio de Economía y Competitividad (BES-2013-064171).

## References

1. Buzsáki G, Leung LWS, Vanderwolf CH. Cellular bases of hippocampal EEG in the behaving rat. Brain Res. 1983; 287:139–171. [PubMed: 6357356]
2. Skaggs WE, et al. EEG sharp waves and sparse ensemble unit activity in the macaque hippocampus. J. Neurophysiol. 2007; 98:898–910. [PubMed: 17522177]
3. Kamondi A, Acsády L, Buzsáki G. Dendritic spikes are enhanced by cooperative network activity in the intact hippocampus. J. Neurosci. 1998; 18:3919–3928. [PubMed: 9570819]
4. Csicsvari J, Hirase H, Mamiya A, Buzsáki G. Ensemble patterns of hippocampal CA3-CA1 neurons during sharp wave-associated population events. Neuron. 2000; 28:585–594. [PubMed: 11144366]
5. Ylinen A, et al. Sharp wave-associated high-frequency oscillation (200 Hz) in the intact hippocampus: network and intracellular mechanisms. J. Neurosci. 1995; 15:30–46. [PubMed: 7823136]
6. Klausberger T, et al. Brain state- and cell type-specific firing of hippocampal interneurons *in vivo*. Nature. 2003; 421:844–848. [PubMed: 12594513]
7. Klausberger T, et al. Complementary roles of cholecystokinin- and parvalbumin-expressing GABAergic neurons in hippocampal network oscillations. J. Neurosci. 2005; 25:9782–9793. [PubMed: 16237182]
8. Maier N, et al. Coherent phasic excitation during hippocampal ripples. Neuron. 2011; 72:137–152. [PubMed: 21982375]
9. English DF, et al. Excitation and inhibition compete to control spiking during hippocampal ripples: intracellular study in behaving mice. J. Neurosci. 2014; 34:16509–16517. [PubMed: 25471587]
10. Slomianka L, Amrein I, Knuesel I, Sørensen JC, Wolfer DP. Hippocampal pyramidal cells: the reemergence of cortical lamination. Brain Struct. Funct. 2011; 216:301–317. [PubMed: 21597968]
11. Dong H-W, Swanson LW, Chen L, Fanselow MS, Toga AW. Genomic-anatomic evidence for distinct functional domains in hippocampal field CA1. Proc. Natl. Acad. Sci. USA. 2009; 106:11794–11799. [PubMed: 19561297]
12. Baimbridge KG, Peet MJ, McLennan H, Church J. Bursting response to current-evoked depolarization in rat CA1 pyramidal neurons is correlated with lucifer yellow dye coupling but not with the presence of calbindin-D28k. Synapse. 1991; 7:269–277. [PubMed: 2042109]
13. Bannister NJ, Larkman AU. Dendritic morphology of CA1 pyramidal neurones from the rat hippocampus. I. Branching patterns. J. Comp. Neurol. 1995; 360:150–160. [PubMed: 7499560]
14. Nielsen JV, Blom JB, Noraberg J, Jensen NA. Zbtb20-Induced CA1 pyramidal neuron development and area enlargement in the cerebral midline cortex of mice. Cereb. Cortex. 2010; 20:1904–1914. [PubMed: 19955470]
15. Kohara K, et al. Cell type-specific genetic and optogenetic tools reveal hippocampal CA2 circuits. Nat. Neurosci. 2014; 17:269–279. [PubMed: 24336151]
16. Lee SH, et al. Parvalbumin-positive basket cells differentiate among hippocampal pyramidal cells. Neuron. 2014; 82:1129–1144. [PubMed: 24836505]
17. Mizuseki K, Diba K, Pastalkova E, Buzsáki G. Hippocampal CA1 pyramidal cells form functionally distinct sublayers. Nat. Neurosci. 2011; 14:1174–1181. [PubMed: 21822270]

18. Senior TJ, Huxter JR, Allen K, O'Neill J, Csicsvari J. Gamma oscillatory firing reveals distinct populations of pyramidal cells in the CA1 region of the hippocampus. J. Neurosci. 2008; 28:2274–2286. [PubMed: 18305260]
19. Stark E, et al. Pyramidal cell-interneuron interactions underlie hippocampal ripple oscillations. Neuron. 2014; 83:467–480. [PubMed: 25033186]
20. O'Neill J, Senior T, Csicsvari J. Place-selective firing of CA1 pyramidal cells during sharp wave/ripple network patterns in exploratory behavior. Neuron. 2006; 49:143–155. [PubMed: 16387646]
21. Fritschy JM, Harvey RJ, Schwarz G. Gephyrin: where do we stand, where do we go? Trends Neurosci. 2008; 31:257–264. [PubMed: 18403029]
22. Freund TF, Buzsáki G. Interneurons of the hippocampus. Hippocampus. 1996; 6:347–470. [PubMed: 8915675]
23. Katona I, et al. Presynaptically located CB1 cannabinoid receptors regulate GABA release from axon terminals of specific hippocampal interneurons. J. Neurosci. 1999; 19:4544–4558. [PubMed: 10341254]
24. Takács VT, Szonyi A, Freund TF, Nyiri G, Gulyás AI. Quantitative ultrastructural analysis of basket and axo-axonic cell terminals in the mouse hippocampus. Brain Struct. Funct. 2015; 220:919–940. [PubMed: 24407853]
25. Glickfeld LL, Atallah BV, Scanziani M. Complementary modulation of somatic inhibition by opioids and cannabinoids. J. Neurosci. 2008; 28:1824–1832. [PubMed: 18287499]
26. Bartos M, Elgueta C. Functional characteristics of parvalbumin- and cholecystokinin-expressing basket cells. J. Physiol. (Lond.). 2012; 590:669–681. [PubMed: 22250212]
27. Chevaleyre V, Siegelbaum SA. Strong CA2 pyramidal neuron synapses define a powerful disynaptic cortico-hippocampal loop. Neuron. 2010; 66:560–572. [PubMed: 20510860]
28. Tukker JJ, Fuentealba P, Hartwich K, Somogyi P, Klausberger T. Cell type-specific tuning of hippocampal interneuron firing during gamma oscillations in vivo. J. Neurosci. 2007; 27:8184–8189. [PubMed: 17670965]
29. Korshunov VA. Miniature microdrive for extracellular recording of neuronal activity in freely moving animals. J. Neurosci. Methods. 1995; 57:77–80. [PubMed: 7791367]
30. Lapray D, et al. Behavior-dependent specialization of identified hippocampal interneurons. Nat. Neurosci. 2012; 15:1265–1271. [PubMed: 22864613]
31. Roumis DK, Frank LM. Hippocampal sharp-wave ripples in waking and sleeping states. Curr. Opin. Neurobiol. 2015; 35:6–12. [PubMed: 26011627]
32. Varga C, Golshani P, Soltesz I. PNAS Plus: Frequency-invariant temporal ordering of interneuronal discharges during hippocampal oscillations in awake mice. Proc. Natl. Acad. Sci. USA. 2012; 109:E2726–E2734. [PubMed: 23010933]
33. Katona L, et al. Sleep and movement differentiates actions of two types of somatostatin-expressing gabaergic interneuron in rat hippocampus. Neuron. 2014; 82:872–886. [PubMed: 24794095]
34. Ellender TJ, Nissen W, Colgin LL, Mann EO, Paulsen O. Priming of hippocampal population bursts by individual perisomatic-targeting interneurons. J. Neurosci. 2010; 30:5979–5991. [PubMed: 20427657]
35. Bähner F, et al. Cellular correlate of assembly formation in oscillating hippocampal networks *in vitro*. Proc. Natl. Acad. Sci. USA. 2011; 108:E607–E616. [PubMed: 21768381]
36. Aivar P, Valero M, Bellistri E, Menendez de la Prida L. Extracellular calcium controls the expression of two different forms of ripple-like hippocampal oscillations. J. Neurosci. 2014; 34:2989–3004. [PubMed: 24553939]
37. Lee D, Lin B-J, Lee AK. Hippocampal place fields emerge upon single-cell manipulation of excitability during behavior. Science. 2012; 337:849–853. [PubMed: 22904011]
38. Bland BH, Konopacki J, Dyck R. Heterogeneity among hippocampal pyramidal neurons revealed by their relation to theta-band oscillation and synchrony. Exp. Neurol. 2005; 195:458–474. [PubMed: 16023636]
39. Bodor AL, et al. Endocannabinoid signaling in rat somatosensory cortex: laminar differences and involvement of specific interneuron types. J. Neurosci. 2005; 25:6845–6856. [PubMed: 16033894]

Europe PMC Funders Author Manuscripts


40. Glickfeld LL, Scanziani M. Distinct timing in the activity of cannabinoid-sensitive and cannabinoid-insensitive basket cells. Nat. Neurosci. 2006; 9:807–815. [PubMed: 16648849]
41. Lenkey N, et al. Tonic endocannabinoid-mediated modulation of GABA release is independent of the CB1 content of axon terminals. Nat. Commun. 2015; 6:6557. [PubMed: 25891347]
42. Cea-del Rio CA, et al. M3 muscarinic acetylcholine receptor expression confers differential cholinergic modulation to neurochemically distinct hippocampal basket cell subtypes. J. Neurosci. 2010; 30:6011–6024. [PubMed: 20427660]
43. Dupret D, O'Neill J, Pleydell-Bouverie B, Csicsvari J. The reorganization and reactivation of hippocampal maps predict spatial memory performance. Nat. Neurosci. 2010; 13:995–1002. [PubMed: 20639874]
44. Mercer A, Trigg HL, Thomson AM. Characterization of neurons in the CA2 subfield of the adult rat hippocampus. J. Neurosci. 2007; 27:7329–7338. [PubMed: 17611285]
45. Viney TJ, et al. Network state-dependent inhibition of identified hippocampal CA3 axo-axonic cells *in vivo*. Nat. Neurosci. 2013; 16:1802–1811. [PubMed: 24141313]
46. Klausberger T, Somogyi P. Neuronal diversity and temporal dynamics: the unity of hippocampal circuit operations. Science. 2008; 321:53–57. [PubMed: 18599766]
47. Worrell GA, et al. High-frequency oscillations in human temporal lobe: simultaneous microwire and clinical macroelectrode recordings. Brain. 2008; 131:928–937. [PubMed: 18263625]
48. Jefferys JGR, et al. Mechanisms of physiological and epileptic HFO generation. Prog. Neurobiol. 2012; 98:250–264. [PubMed: 22420980]
49. Alvarado-Rojas C, et al. Different mechanisms of ripple-like oscillations in the human epileptic subiculum. Ann. Neurol. 2015; 77:281–290. [PubMed: 25448920]
50. Morris ME, Baimbridge KG, El-Beheiry H, Obrocea GV, Rosen AS. Correlation of anoxic neuronal responses and calbindin-D(28k) localization in stratum pyramidale of rat hippocampus. Hippocampus. 1995; 5:25–39. [PubMed: 7787944]
51. Pinault D. A novel single-cell staining procedure performed *in vivo* under electrophysiological control: morpho-functional features of juxtacellularly labeled thalamic cells and other central neurons with biocytin or Neurobiotin. J. Neurosci. Methods. 1996; 65:113–136. [PubMed: 8740589]
52. Sloviter RS. Calcium-binding protein (calbindin-D28k) and parvalbumin immunocytochemistry: localization in the rat hippocampus with specific reference to the selective vulnerability of hippocampal neurons to seizure activity. J. Comp. Neurol. 1989; 280:183–196. [PubMed: 2925892]
53. Airaksinen MS, et al. Ataxia and altered dendritic calcium signaling in mice carrying a targeted null mutation of the calbindin D28k gene. Proc. Natl. Acad. Sci. USA. 1997; 94:1488–1493. [PubMed: 9037080]
54. Celio MR, et al. Monoclonal antibodies directed against the calcium binding protein Calbindin D-28k. Cell Calcium. 1990; 11:599–602. [PubMed: 2285928]
55. San Antonio A, Liban K, Ikrar T, Tsyganovskiy E, Xu X. Distinct physiological and developmental properties of hippocampal CA2 subfield revealed by using anti-Purkinje cell protein 4 (PCP4) immunostaining. J. Comp. Neurol. 2014; 522:1333–1354. [PubMed: 24166578]
56. Pfeiffer F, Simler R, Grenningloh G, Betz H. Monoclonal antibodies and peptide mapping reveal structural similarities between the subunits of the glycine receptor of rat spinal cord. Proc. Natl. Acad. Sci. USA. 1984; 81:7224–7227. [PubMed: 6095276]
57. Feng G, et al. Dual requirement for gephyrin in glycine receptor clustering and molybdoenzyme activity. Science. 1998; 282:1321–1324. [PubMed: 9812897]
58. Schwaller B, et al. Prolonged contraction-relaxation cycle of fast-twitch muscles in parvalbumin knockout mice. Am. J. Physiol. 1999; 276:C395–C403. [PubMed: 9950767]
59. Fukudome Y, et al. Two distinct classes of muscarinic action on hippocampal inhibitory synapses: M2-mediated direct suppression and M1/M3-mediated indirect suppression through endocannabinoid signalling. Eur. J. Neurosci. 2004; 19:2682–2692. [PubMed: 15147302]
60. Takeda K, et al. WFS1 (Wolfram syndrome 1) gene product: predominant subcellular localization to endoplasmic reticulum in cultured cells and neuronal expression in rat brain. Hum. Mol. Genet. 2001; 10:477–484. [PubMed: 11181571]

61. Paxinos, G.; Watson, C. The Rat Brain in Stereotaxic Coordinates. 5th edn.. Elsevier; London: 2005.

62. Schneider CA, Rasband WS, Eliceiri KW. NIH Image to ImageJ: 25 years of image analysis. Nat. Methods. 2012; 9:671–675. [PubMed: 22930834]

63. van Betteray JN, Vossen JM, Coenen AM. Behavioural characteristics of sleep in rats under different light/dark conditions. Physiol. Behav. 1991; 50:79–82. [PubMed: 1946735]

64. Pérez-Escudero A, Vicente-Page J, Hinz RC, Arganda S, de Polavieja GG. idTracker: tracking individuals in a group by automatic identification of unmarked animals. Nat. Methods. 2014; 11:743–748. [PubMed: 24880877]



Europe PMC Funders Author Manuscripts

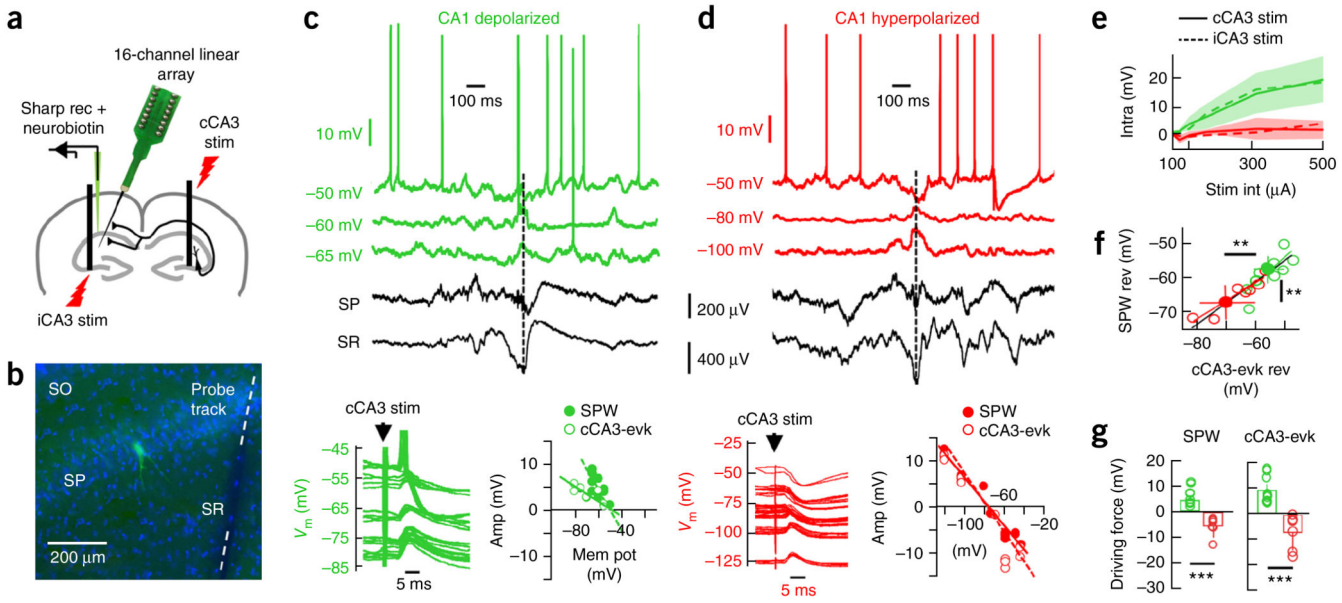


**Figure 1.**

Heterogeneous responses of dorsal CA1 PCs during SPW ripples *in vivo*. (**a**) Summary of the experimental approach. CA1 PCs impaled with sharp pipettes were recorded simultaneously to local field potentials using 16-channel silicon probes in urethane anesthetized rats. cCA3 and iCA3 stimulation were applied to evaluate cell responses. (**b**) Subsequent morphological analysis allowed for evaluation of cell identity (green) and distance to probe track. Blue is bisbenzimide. (**c**) Representative CA1 PC exhibiting net depolarization during SPW ripples recorded at the stratum radiatum (SR) and pyramidale (SP). A discontinuous line marks the SPW peak used for alignment. Responses to cCA3 stimulation are shown at bottom (left), and the reversal potential estimation of the SPW-associated and cCA3-evoked (cCA3-evk) response are shown on the right. (**d**) Data are presented as in **c** for a representative hyperpolarized PC. (**e**) Group difference of input/output responses of hyperpolarized (red) and depolarized (green) cells to contralateral (solid; $n = 7$ red, $n = 11$ green) and ipsilateral (discontinuous; $n = 4$ red, $n = 4$ green) CA3 stimulation. Lines reflect mean values. s.d. values for iCA3 stimulation are shadowed. (**f**) Reversal potential of SPW- and cCA3-evoked responses were tightly correlated ($P < 0.0001$, $r(16) = 89.25$; Pearson correlation), but different between groups (SPW-reversal: $P = 0.0041$, $t(19) = 3.27$; cCA3-evoked reversal: $P = 0.0067$, $t(16) = 3.11$; $n = 11$ depolarized, $n = 7$ hyperpolarized cells; unpaired $t$ test). Solid circles represent group mean ± s.d. (**g**) Significant group differences for SPW- (left, $P < 0.0001$) and cCA3-evoked driving forces ($P < 0.0001$). $^{**}P < 0.005$, $^{***}P < 0.0001$.




Europe PMC Funders Author Manuscripts

Europe PMC Funders Author Manuscripts

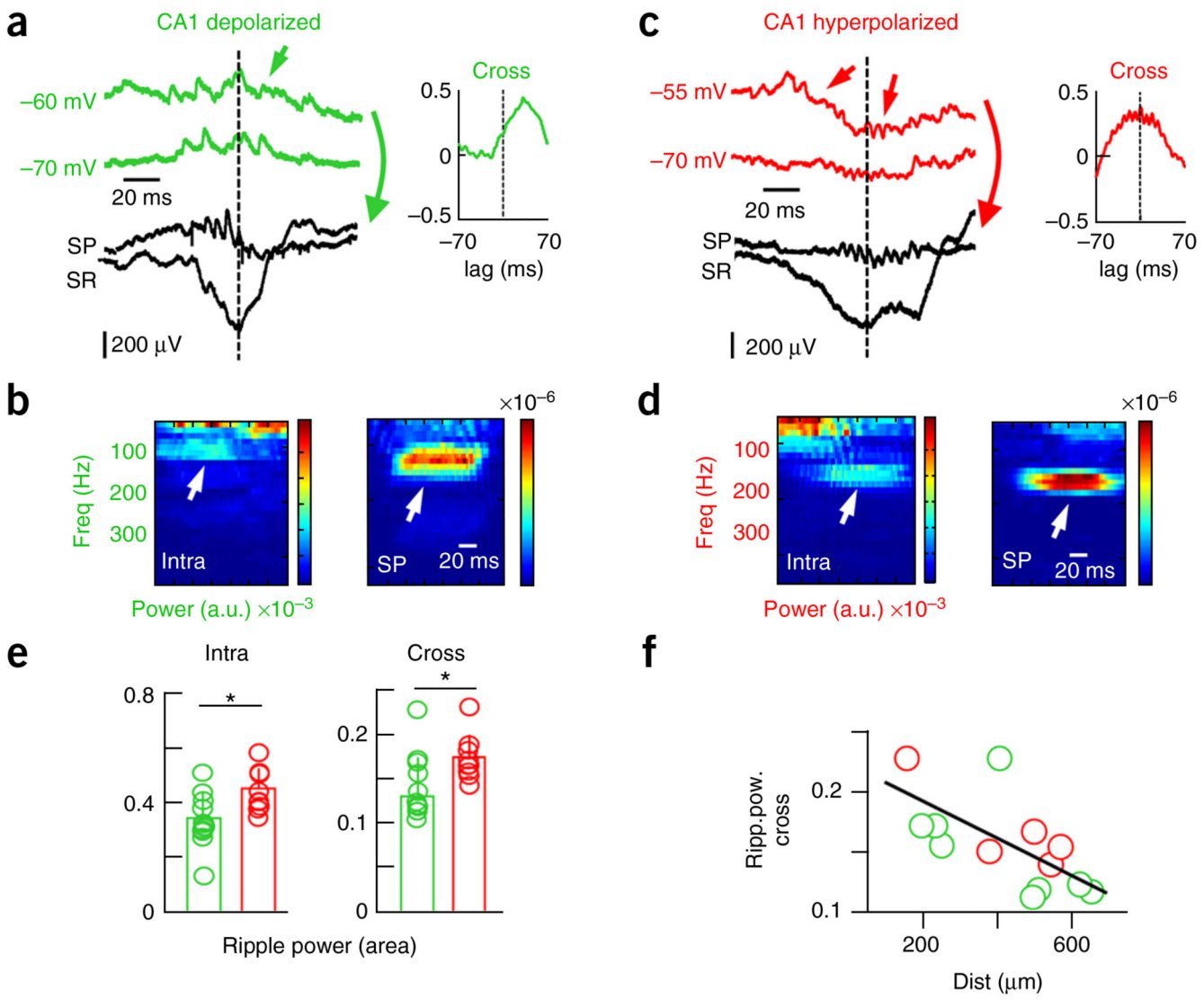


**Figure 2.**

Different correlation between intracellular and extracellular ripples in depolarized and hyperpolarized CA1 PCs. (**a**) Representative synaptic activity during SPW ripples in depolarized cells. (**b**) Time frequency spectrum of intracellular sweeps (green, arrows in **a**) suggested a contribution to the ripple frequency band simultaneously with the extracellular ripple recorded at the stratum pyramidale (black, SP). A cross-correlation analysis revealed coherent high-frequency oscillations between the intracellular and the extracellular ripple (shown at right in **a**). (**c**) Data are presented as in **a** for a representative hyperpolarized PC. (**d**) Data are presented as in **b** for the sweeps shown in **c** (arrows). (**e**) Group data of the mean ripple power confirmed stronger intracellular rhythmicity ($P = 0.0124$, $t(19) = -2.8$, left) and intra-extra ripple cross-correlation ($P = 0.0147$, $t(19) = -2.7$, right) in hyperpolarized ($n = 12$) versus depolarized ($n = 9$) cells. (**f**) Relationship between intra-extra ripple cross-correlation and the recording distance between the cell and the 16-channel probe ($P = 0.0137$, $r(12) = -0.6401$; Pearson correlation). *$P < 0.05$.

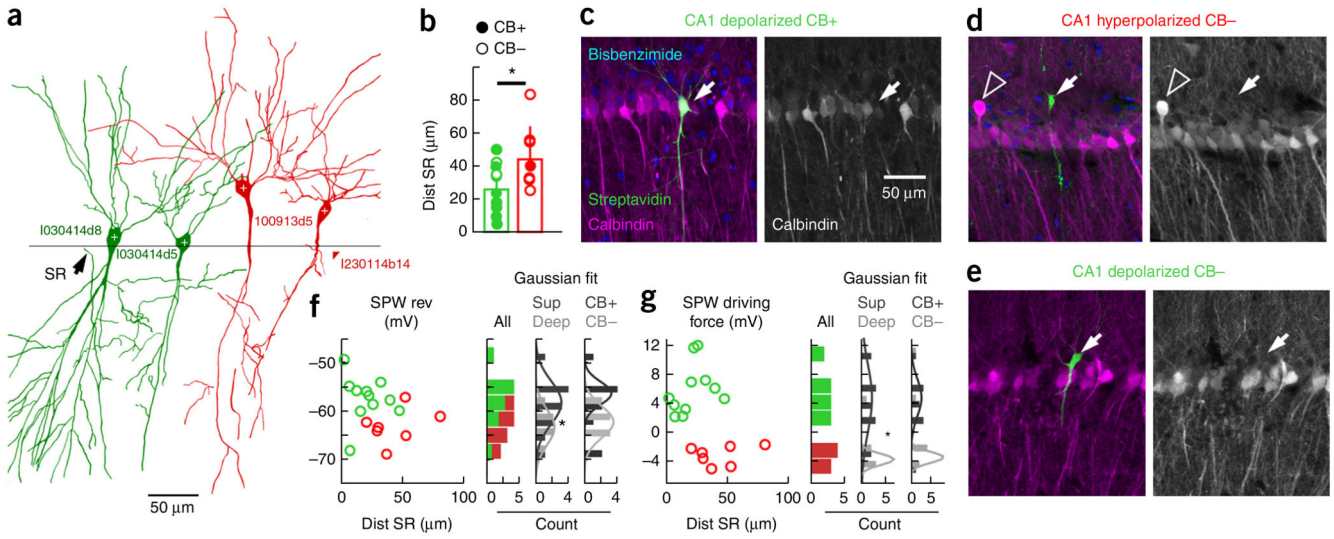


**Figure 3.**

Identity of depolarized and hyperpolarized CA1 PCs. (**a**) Camera lucida drawing of DAB-revealed cells (1 section, 70 µm, 40×). The border between strata pyramidale and radiatum (line) was identified. (**b**) Group differences in the distance to stratum radiatum (SR, $P = 0.0152$, $t(16) = -2.72$; green, $n = 11$ depolarized; red, $n = 7$ hyperpolarized). CB immunoreactivity (CB+, filled dots) and the lack thereof (CB−, open) is indicated. (**c**) Example of a superficial depolarized CB+ cell (arrows) recorded close to radiatum and in the CB+ sublayer. Average intensity projection (five optical sections, 9.44 µm). (**d**) Example of a deep hyperpolarized CB− cell (arrows) located above the CB+ sublayer. Note the deep CB+ cells (open arrowhead, 12 optical sections, 11.88 µm). (**e**) Example of a deep depolarized CB− cell (arrow, 8 optical sections, 14.1 µm). (**f**) Relationship between the SPW-associated reversal potential and the cell distance to radiatum. Histograms for all cells without classification (individual counting from depolarized and hyperpolarized cells is visually identified) and classified according to location (deep/superficial) and immunoreactivity (CB+/CB−) are shown to the right. A Gaussian fit was tested (Shapiro-Wilk test) for deep ($P = 0.9859$, W = 0.99) and superficial ($P = 0.9378$, W = 0.97) PCs and means were significant different ($P = 0.0405$, $t(16) = 1.86$, unpaired *t* test). Differences did not reach significance for CB classification (CB+: $P = 0.1394$, W = 0.88; CB−: $P = 0.8568$, W = 0.96; $P = 0.0923$, $t(16) = 1.38$, unpaired *t* test, not significant). (**g**) Data are presented as in **d** for SPW-associated driving force values (deep: $P = 0.0675$, W = 0.81; superficial: $P = 0.6691$, W = 0.95; means were significantly different, $P = 0.0135$, rank sum = 140, Mann-Whitney; CB+: $P = 0.2403$, W = 0.91; CB−: $P = 0.0113$, W = 0.74; n.s.). $^{*}P < 0.05$.




Europe PMC Funders Author Manuscripts

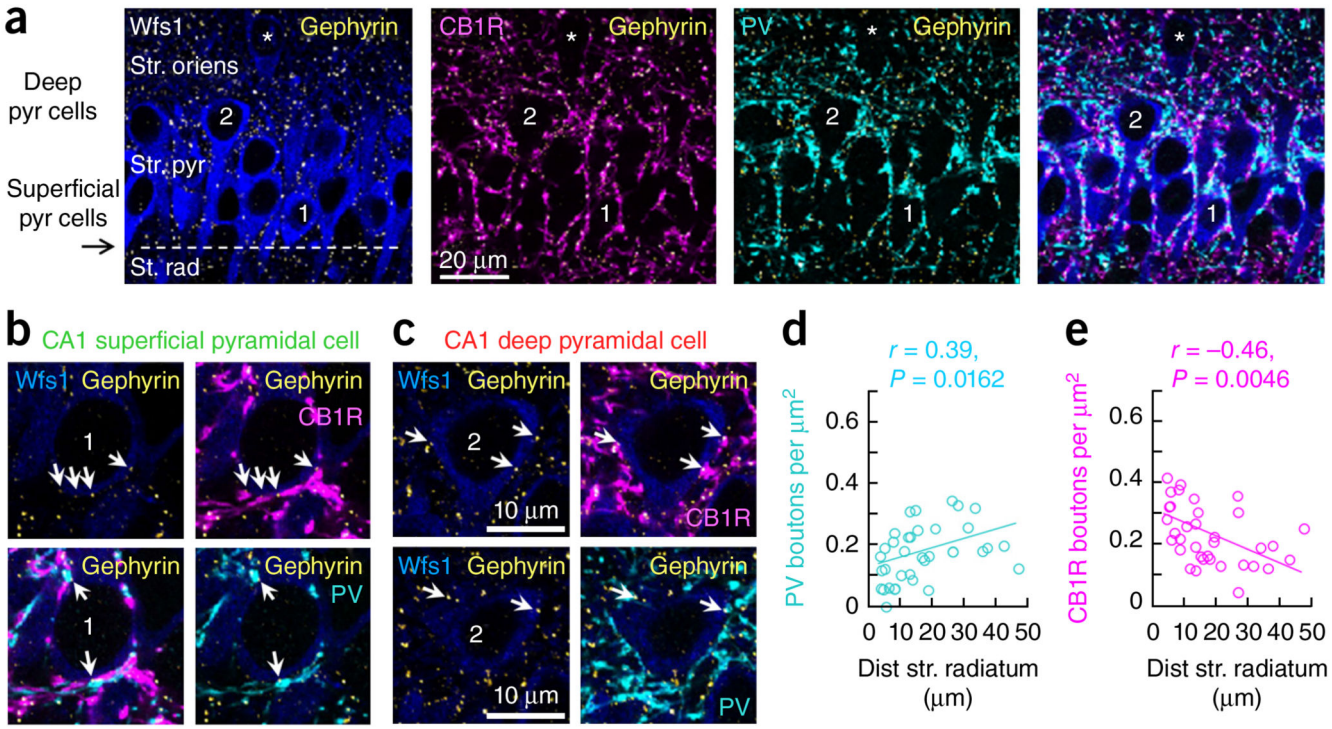


**Figure 4.**

GABAergic perisomatic innervation of CA1 pyramidal cells. (**a**) Average intensity projection (five optical sections, 1.43 µm thick) of CA1 pyramidal cells immunoreactive for Wfs1 (blue). A typical superficial pyramidal cell close to the border with radiatum is marked 1. Cell 2 is a deep pyramidal cell. An example of oriens pyramidal cells (also counted as deep) is highlighted by an asterisk. Gephyrin immunolabeling allowed identification of GABAergic puncta (yellow). CB1R− (magenta) and PV-immunoreactive (cyan) terminals surrounded pyramidal cell somata and dendrites. (**b**) Superficial layer cell 1 from **a** (single 0.29-µm-thick optical section). Both PV (cyan) and CB1R (magenta) terminals were associated with gephyrin puncta (yellow, arrows) on the Wfs1-immunoreactive soma (blue). Top row, four gephyrin puncta and corresponding CB1R-immunoreactive terminals (arrows). Bottom row, two gephyrin puncta (arrows) associated with PV-immunoreactive terminals. (**c**) Data are presented as in **b** for deep layer cell 2 from **b** shown in single 0.29-µm-thick optical sections at two different depths. (**d**) Estimation of the density of PV+/gephyrin puncta over all Wfs1 pyramidal cells revealed a significant positive correlation with the distance to radiatum ($n$ = 34 cells, 4 confocal stacks, $n$ = 3 rats). (**e**) An opposite trend was found for CB1R+/gephyrin puncta in the same dataset.

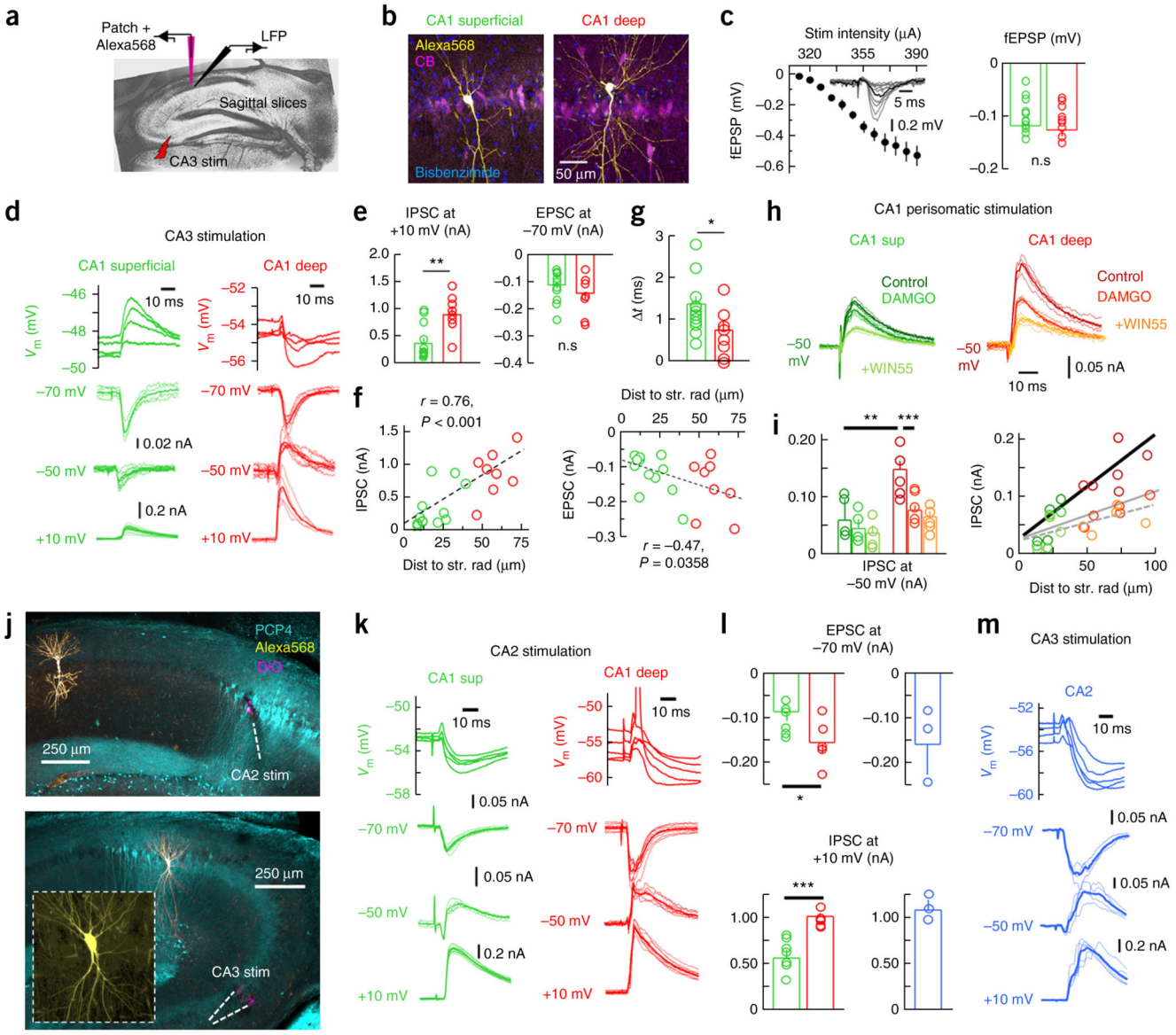


**Figure 5.**

Mechanisms of CA1 PC heterogeneity studied *in vitro*. (**a**) Schematic representation of *in vitro* experiments. (**b**) Classification of CA1 PCs as deep and superficial. Average intensity projection from three (7.66 µm, deep) and seven optical sections (19.86 µm, superficial). (**c**) Stimulation intensity (inset, radiatum field excitatory postsynaptic potentials (fEPSP)) was adjusted to obtain similar fEPSPs in slices used to evaluate deep ($n = 8$) and superficial cells ($n = 12$, $P = 0.6831$, right). (**d**) Representative current- and voltage-clamp responses of deep and superficial CA1 PCs to CA3 stimulation. (**e**) Stronger ISPCs were evoked in deep PCs at +10 mV ($P = 0.0021$, $t(18) = -3.39$; $n = 8$ deep, $n = 12$ superficial). EPSCs at −70 mV was not significant ($P = 0.2221$). (**f**) Correlation between the amplitude of IPSC (left) and EPSC (right) and distance to radiatum. (**g**) Group differences of onset timing between excitation and inhibition ($P = 0.0431$, $t(18) = -2.18$). (**h**) Evaluation of perisomatic stimulation




Europe PMC Funders Author Manuscripts

responses in deep and superficial PCs. Representative responses to perfusion with the μ-opioid receptor antagonist DAMGO (200 nM) and the CB1R agonist WIN55,212 (5 μM). (**i**) IPSC amplitude measured at −50 mV in deep ($n = 5$) and superficial PCs ($n = 4$) in response to pharmacological interventions. $^{**}P = 0.0061$, $t(7) = -3.87$; $^{***}P = 0.0055$, $t(4) = 5.44$. The relationship between the IPSC amplitude and the distance to radiatum (control, thick line, $r = 0.86$, $P = 0.0012$) was reduced by DAMGO (gray continuous line, $r = 0.78$, $P = 0.0131$) and remained non-significant after WIN55,212 (discontinuous line). (**j**) Confirmation of CA2 stimulation with DiO and PCP4 immunolabeling. Bottom, confirmation of CA2 PC identity. Images were taken at 10×. Inset, 40×. (**k**) Representative responses of deep and superficial CA1 PCs to CA2 stimulation. (**l**) Deep ($n = 5$) and superficial ($n = 7$) CA1 PC responses to CA2 stimulation (EPSCs: $P = 0.0474$, $t(10) = -2.25$; IPSCs: $P = 0.0007$, $t(10) = 4.81$). Right, similar data from CA2 cells in response to CA3 stimulation (blue, $n = 3$). (**m**) Responses of a representative CA2 pyramidal cell to CA3 stimulation. $^{*}P < 0.05$, $^{**}P < 0.005$, $^{***}P < 0.0001$.





Europe PMC Funders Author Manuscripts

Europe PMC Funders Author Manuscripts

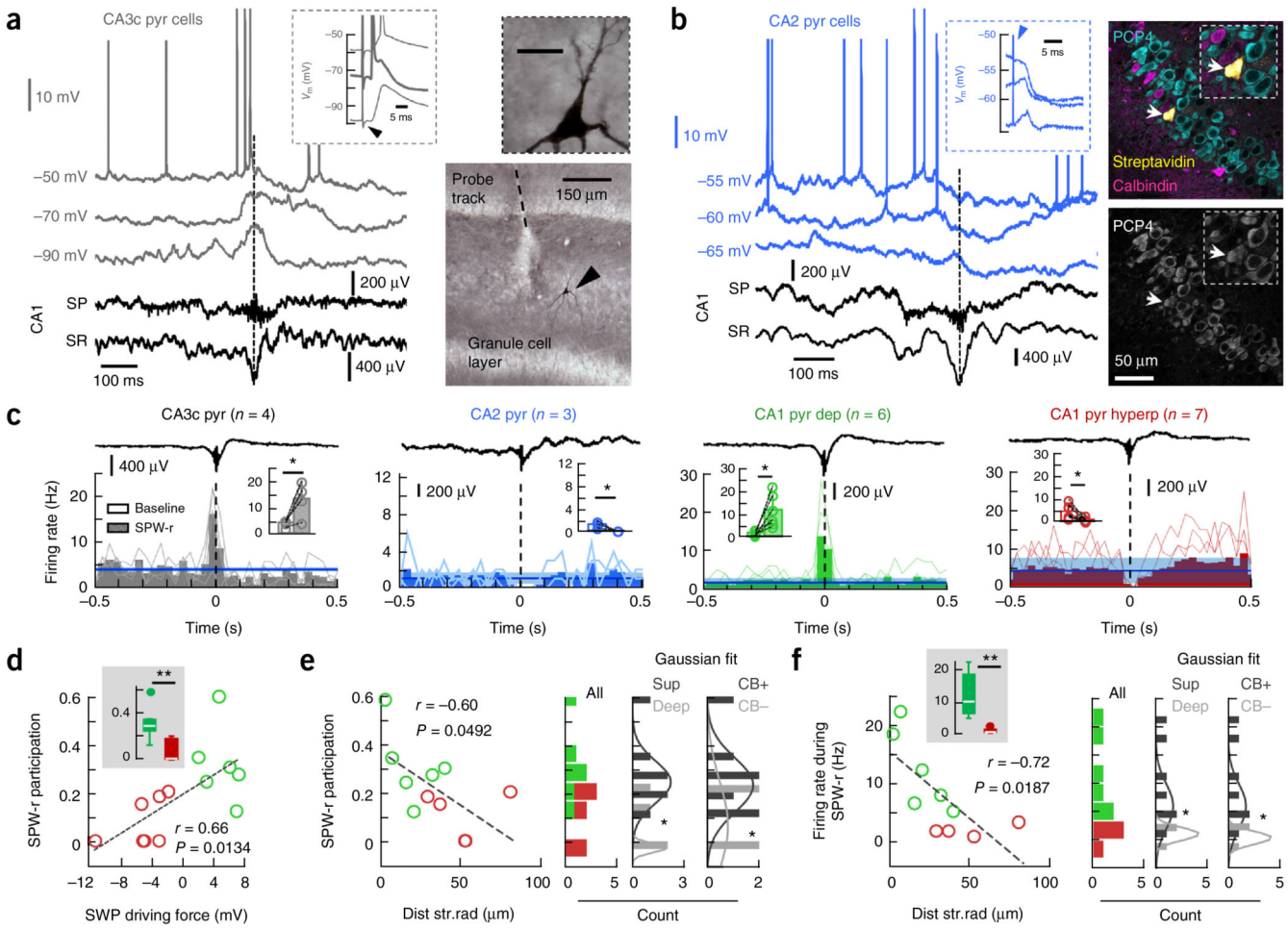


**Figure 6.**

Microcircuit control of SPW-associated responses in dorsal PCs *in vivo*. (**a**) Representative response of a CA3c PC during SPWs recorded in CA1 (discontinuous line). Inset, ortodromic and antidromic (thick line) responses to cCA3 stimulation (arrowhead). Right, cell identification with DAB reaction at 10× and 100× (inset, scale bar represents 20 µm). Note large spines (thorny excrescences). (**b**) Data are presented as in **a** for a representative CA2 PC. Right, validation with PCP4 immunolabeling (arrows, 3 optical sections, 2.92 µm). (**c**) Firing rate histograms (bin size of 30 ms) of PCs recorded along the cornu ammonis at resting membrane potentials are aligned by CA1 SPW ripples. Blue lines represent mean firing rate (s.d. is shadowed) as estimated from baseline (−500 to −400 ms). Insets, firing rate modulation before (baseline) and around SPW peak (60-ms window). CA3c: $P = 0.0464$, $t(3) = -3.27$, $n = 4$; CA2: $P = 0.0441$, $t(2) = 3.13$, $n = 3$; CA1 depolarized: $P = 0.0173$, $t(5) = -3.49$, $n = 6$; CA1 hyperpolarized cells: $P = 0.0275$, $t(6) = 2.89$, $n = 7$. (**d**) Relationship between cell participation of SPW ripples and the associated driving force for all CA1 PCs shown before. Inset, significant group differences ($P = 0.0034$, $t(12) = 3.63$). (**e**) SPW participation against the distance to radiatum in histologically confirmed PCs ($n = 6$ depolarized, $n = 4$ hyperpolarized). Right, histograms from unclassified cells (all) and classified according to location (deep/superficial) and immunoreactivity (CB+/CB−) tested

against a Gaussian distribution (Shapiro-Wilk test). Deep: $P = 0.1612$, W = 0.82; superficial: $P = 0.1609$, W = 0.87; means are significantly different at $P = 0.0431$, $t(8) = 2.35$, unpaired $t$ test. For CB+: $P = 0.1749$, W = 0.87; CB−: $P = 0.060$, W = 0.77; means are significantly different at $P = 0.0302$, $t(8) = 2.146$ for an unpaired $t$ test, but not for a Mann-Whitney test. (**f**) Data are presented as in **e** for firing rate data. Shapiro-Wilk test for deep: $P = 0.7804$, W = 0.98; superficial: $P = 0.5954$, W = 0.93; means are significantly different at $P = 0.043$, $t(8) = 1.94$, unpaired $t$ test. For CB+: $P = 0.5954$, W = 0.93; CB−: $P = 0.7804$, W = 0.98; means are significantly different at $P = 0.043$, $t(8) = 1.94$, unpaired $t$ test. $^{*}P < 0.05$, $^{**}P < 0.005$, $^{***}P < 0.0001$.



Europe PMC Funders Author Manuscripts

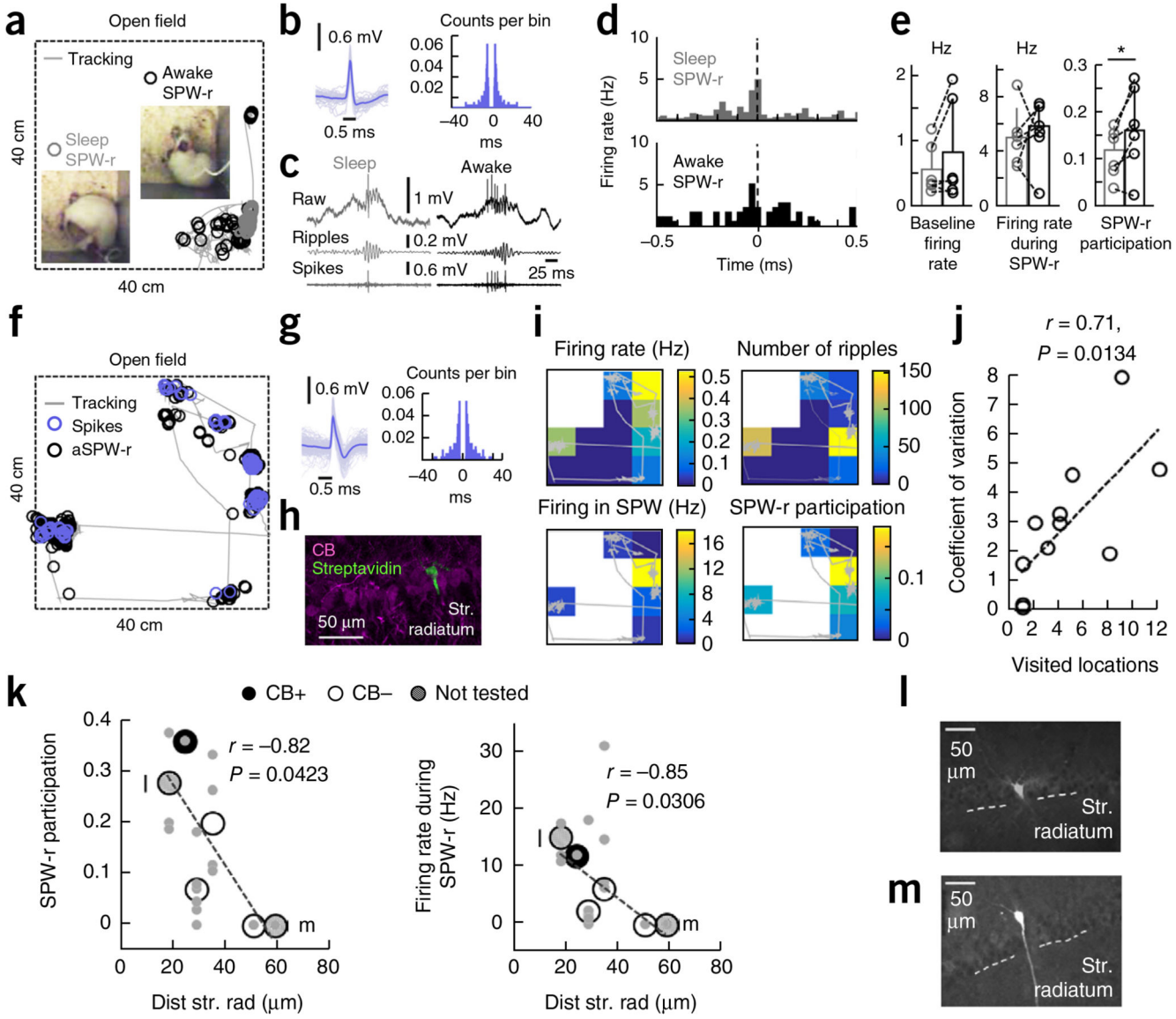


**Figure 7.**

CA1 PC participation during SPW ripples in drug-free conditions. (**a**) Single-cell recording of CA1 PCs and LFPs in freely moving rats enabled identification of activity patterns during sleep (gray) and awake (black) conditions. Insets, representative behavior. (**b**) Action potential waveform and firing autocorrelogram of the cell recorded from the rat shown in **a**. (**c**) Representative examples of sleep and awake SPW ripples. Ripples: 100–200-Hz filtered raw signal; spikes: high-pass signals at 300 Hz. (**d**) Firing rate histograms (30-ms bins) of the cell shown before for all SPW ripples recorded during sleep (221) and awake (60). (**e**) State-dependent effects were not significant for the baseline firing rate ($P = 0.1887$, $t(5) = -1.52$) or the firing rate during SWP ripples ($P = 0.8661$, $t(5) = -0.18$), but reached significance for SPW ripple participation ($P = 0.0420$, $t(5) = -2.71$; $n = 6$ CA1 PCs, 1 histologically confirmed). *$P < 0.05$. (**f**) Recordings obtained from freely moving rats also allowed us to examine spatial effects in awake SPW ripple participation (black). Spikes are




Europe PMC Funders Author Manuscripts

shown in blue. (**g**) Spike waveform and autocorrelation of the cell recorded in **f**. (**h**) Juxtacellular labeling and *post hoc* identification of the cell in **g** confirmed it was a deep CB − PC (3 optical sections, 6 μm). (**i**) Spatial dependence of activity of cell shown in **g**. (**j**) Relationship between the coefficient of variation of the firing rate during awake SPW ripples and the number of visited locations (4 × 4) in the 40-cm × 40-cm arena ($n$ = 11 cells, 6 histologically confirmed). (**k–m**) Participation (left) and firing rate (right) during SPW ripples against the distance to radiatum for histologically confirmed cells ($n$ = 6). Values represent means for the entire recording session. Individual values during different states (awake, sleep) and spatial locations for each cell are shown in gray. Calbindin classification is shown, except for two not tested cells indicated in by letters and shown in **l** and **m**.



Europe PMC Funders Author Manuscripts